C. R. Mecanique 346 (2018) 724–742

Contents lists available at ScienceDirect

Comptes Rendus Mecanique

www.sciencedirect.com

Computational modelling of material forming processes / Simulation numérique des procédés de mise en forme

Multiscale modelling of asymmetric rolling with an anisotropic constitutive law

Diarmuid Shore [a], Paul Van Houtte [a], Dirk Roose [c], Albert Van Bael [a,b,*]

[a] KU Leuven, Department of Materials Engineering, Kasteelpark Arenberg 44 Box 2450, B-3001 Leuven, Belgium
[b] KU Leuven, Materials Technology TC, Campus Diepenbeek, Agoralaan Gebouw B Box 8, B-3590 Diepenbeek, Belgium
[c] KU Leuven, Department of Computer Science, Celestijnenlaan 200A, B-3001 Leuven, Belgium

ARTICLE INFO

Article history:
Received 30 October 2017
Accepted 20 April 2018
Available online 27 June 2018

Keywords:
Non-linear plasticity
Anisotropy
Texture
Finite element methods

ABSTRACT

A parametric study is presented, which employs a new anisotropic constitutive law in order to study the influence of anisotropic plasticity on the deformation field of the Asymmetric Rolling (ASR) process. A version of the FACET method is presented, where an analytical yield function is restricted to the subspace of the stress and strain rate space relevant for 2D Finite Element Analysis (FEA), but can still accurately reproduce the plastic anisotropy of an underlying Crystal Plasticity (CP) model. The influence of anisotropy on the deformation field and corresponding texture evolution is examined in terms of the changes in texture component volume fractions and formation of texture gradients. It is found that a material with the anisotropy of a sharp cold-rolled aluminium alloy is more beneficial than that of a recrystallised hot-rolled aluminium alloy, and this influence of anisotropy suggests that Asymmetric Rolling (ASR) may be best carried out in the latest stages of cold rolling.

1. Introduction

1.1. Aluminium alloys for automotive bodywork

Aluminium alloys are recently gaining importance as a versatile material in the drive to reduce emissions and increase fuel efficiency of passenger vehicles. For example, the “Super Light Car” project, sponsored by the European Council For Automotive Research (EUCAR) resulted in a design concept with more than 50% (by weight) of aluminium alloys in an application engineered material approach to vehicle weight reduction [1]; aluminium alloy bodywork has also already been used successfully in some mass-produced vehicles such as the Ford F150. However, one of the difficulties in replacing steel with aluminium alloys in automotive bodywork is their lower formability, which arises in part from their characteristic plastic anisotropy, which in turn is closely related to their crystallographic texture [2].

In general the 5XXX series alloys are employed in inner panels due to their better formability, while the 6XXX series alloys are almost exclusively used for outer panels where formability is to some degree traded for the ability to increase the yield strength after forming by precipitation hardening. Precipitation hardening is crucial to providing the necessary dent resistance [3]. The main alloying elements in the 6000 series alloys, namely Mg and Si, have strong solid-solution, dispersion

* Corresponding author at: KU Leuven, Department of Materials Engineering, Kasteelpark Arenberg 44 Box 2450, B-3001, Leuven, Belgium.
E-mail address: albert.vanbael@kuleuven.be (A. Van Bael).

https://doi.org/10.1016/j.crme.2018.06.001
1631-0721/

Abbreviations

ODF	Orientation Distribution Function	**NNLS**	Non Negative Least Squares
API	Application Programming Interface	**OIM**	Orientation Imaging Microscopy
ASR	Asymmetric Rolling	**PSN**	Particle Stimulated Nucleation
CP	Crystal Plasticity	**RD**	Rolling Direction
CPFEM	Crystal Plasticity Finite Element Method	**SR**	Symmetric Rolling
EUCAR	European Council for Automotive Research	**TBH**	Taylor–Bishop–Hill
FE	Finite Element	**TD**	Transverse Direction
FEA	Finite Element Analysis	**UTS**	Ultimate Tensile Strength
LDH	Limiting Dome Height	**XRD**	X-Ray Diffraction
LDR	Limiting Drawing Ratio	**CPFFT**	Crystal Plasticity Fast Fourier Transform
ND	Normal Direction		

and precipitation (age) hardening effects. In addition, these elements inhibit recovery, which increases the strain hardening rate [4].

In general, 6016 is currently valued for formability and corrosion resistance, while 6111 is more favoured in the US for its higher Ultimate Tensile Strength (UTS) after ageing, as typically thinner sheet gauges (0.9–1.0 mm) are employed there [3]. While the nominal compositions of these alloys do allow producers some flexibility to adjust the mechanical properties and heat treatability, ultimately quite specific compositions are required to obtain an optimal combination of low-yield strength before forming and high-yield strength after the paint bake cycle [5]. This motivates research into mechanical processing techniques that can improve material properties, such as formability, without altering composition.

1.2. Formability, anisotropy, and texture

The formability of a sheet metal can be quantified by parameters such as Limiting Dome Height (LDH), Limiting Drawing Ratio (LDR), the direction-averaged normal anisotropy $\bar{r}$ and the power-law strain-hardening exponent n. Stress ratio parameters can be similarly employed, e.g., the ratio P of stress in plane strain tension to the equibiaxial stress [6] or the ratio of stress in plane strain tension to the pure shear stress [7]. Anisotropy parameters such as $\bar{r}$ are of particular interest in the current context, as they can be obtained from multiscale models.

Whiteley [8] attributed the discovery of a correlation between LDR and $\bar{r}$ to Lankford et al. [9],[1] presented the first theoretical analysis in the form of Eq. (1), and suggested that LDR was only weakly correlated with n. The validity of this view has since been upheld by experiment and analyses [10]. The correlation may be explained by considering that increasing the value of $\bar{r}$ should generally increase the proportion of strain occurring in the sheet plane rather than in the thickness, so that the thickness is reduced less rapidly during deformation, and failure is inhibited:

$$\mathrm{LDR} = \exp\left(\mathfrak{f}\sqrt{\frac{1+\bar{r}}{2}}\right) \tag{1}$$

The factor $\mathfrak{f}$ in Eq. (1) is a tuning parameter used to account for the effects of friction, punch geometry, and sheet thickness.[2] A more advanced analysis [11] provides Eq. (2), which extends Eq. (1) to include the influence of n on LDR. Eq. (2) predicts that in the range $0.15 \leq n \leq 0.3$, which accounts for most commercially produced aluminium alloys, LDR is only weakly a function of n, while for fixed values of n the relationship between $\bar{r}$ and LDR is almost linearly increasing. Thus it is reasonable to expect that increasing $\bar{r}$ increases formability in deep drawing:

$$\mathrm{LDR} = \left[\exp\left(2\mathfrak{f}\,\mathrm{e}^{-n}\sqrt{\frac{1+\bar{r}}{2}}\right) + \exp\left(2n\sqrt{\frac{1+\bar{r}}{2}}\right) - 1\right]^{\frac{1}{2}} \tag{2}$$

The anisotropy parameters such as $\bar{r}$ can be determined by mechanical testing, but due to the fact that $\bar{r}$ is a function of the yield surface, it may also be derived numerically from experimental texture measurements by means of a statistical Crystal Plasticity (CP) model [12]. Thus modification of the texture, which in turn results in modification of the yield surface, may be expected to modify $\bar{r}$ and ultimately the formability in deep drawing.

Rolled sheet steels typically feature textures with an α fibre ($\langle 110\rangle \parallel$ Rolling Direction (RD)) and γ fibre ($\langle 111\rangle \parallel$ Normal Direction (ND)); rolled aluminium alloys have quite different textures, typically consisting of the β fibre, (i.e. orientations

[1] I.e. cited by Whiteley [8] as [9].

[2] $\mathfrak{f} = 1.0$ for perfect frictionless cup drawing.

linking the copper $\{112\}\langle 111\rangle$, S3 $\{123\}\langle 63\bar{4}\rangle$ and brass $\{110\}\langle 1\bar{1}2\rangle$ components) and cube $\{100\}\langle 001\rangle$ components. In both cases, the major difference in anisotropy $\bar{r}$ for these two classes of sheet metal is predicted by CP models such as the Taylor–Bishop–Hill (TBH) model [13], or more advanced models such as the ALAMEL model [14,15], primarily on the basis of the texture.

1.3. Modification of texture by asymmetric rolling

Shear deformation is present in conventional continuous Symmetric Rolling (SR) processes, but this shear is usually of negligible magnitude, of opposite sense at the top and bottom surfaces of the sheet, and is often confined to the surface layers. ASR modifies the conventional rolling process so that conditions at the upper and lower sheet surface are intentionally unequal, in order to impose a zone of unidirectional shear deformation throughout the sheet thickness. ASR has been experimentally implemented with (a) differing roll diameters [16–20], (b) differing angular velocities of the rolls [21–27], (c) use of an idle roll [28,29] and (d) roll centre offset [30] (sometimes referred to as "snake" or "serpentine" rolling). Most recent experiments that focus on the utility of ASR for microstructure modification in aluminium alloys use method (a), though method (b) has also been frequently used.

Experiments and CP simulations of ASR focusing on texture modification [15,18,25,28,31–34] show that the shear deformation present in ASR rotates the typical β fibre and cube texture components of sheet aluminium alloys towards the $\{001\}\langle 110\rangle$ (H), $\{111\}\langle 1\bar{1}0\rangle$ (E) and $\{111\}\langle 112\rangle$ (F) components, that components in this texture persist during recrystallisation during annealing, and that this type of texture modification generally leads to improved $\bar{r}$ values.

The mechanics of deformation of ASR has been analysed by the slab method [35–42], though the majority of these studies focus on the prediction of rolling forces and control of sheet curvature. However, it is consistently concluded from such analysis that the shear deformation in ASR tends to increase with increasing difference of roll surface velocities, friction stresses, and rolling reduction.[3]

There are potential practical difficulties with using ASR for beneficial texture modifications in an industrial setting. For example, it is well known that ASR can cause significant sheet curvature, the direction and magnitude of which are a complex function of the friction, reduction, and contact length [43–48]. At the same time, it is claimed that such curvature can be regulated via application of additional bending moments and control of entry/exit angles and coiler tensions [37,49]. An issue that has received much less attention to date is the formation of texture gradients [50,51], which may be problematic, as such gradients can promote strain localisation [52,53] or can lead to production problems such as edge cracking [54].

In summary, it is evident that the deformation field in ASR is a complex function of the process parameters. Furthermore, the occurrence of phenomena such as texture gradients requires an approach that accounts for an inhomogeneous deformation field and considers the mechanics of the evolution of the microstructure.

1.4. Explicit 2D finite element analysis of metal forming

Finite Element Analysis (FEA) of engineering scale press-forming operations for sheet metal parts involve meshes with hundreds or thousands of elements. Such simulations typically involve very large areas of contact relative to the volume of material being deformed. A static implicit solution procedure may not be efficient in this scenario, as each iteration in the solution to a given displacement increment may change the contact conditions significantly and impede or even prevent convergence. A quasi-static analysis using a dynamic explicit procedure may alleviate this problem because there is no updating of the contact conditions during stress integration, and so no change in the contact conditions during an increment [55].

However, with the explicit technique the requirement for numerical stability limits the size of the time increment as a function of the element size and material density. For modelling of sheet metal forming, the time increments are usually in the range 10 ns to 2 μs, which necessitates tens of thousands to hundreds of thousands of increments, even when mass or time scaling is employed. It is crucial then that the material constitutive model is as computationally efficient as possible, because it must be evaluated in every increment in every integration point.

Many metal-forming processes may be satisfactorily modelled with two-dimensional finite element formulations, either assuming plane stress (e.g., forming of thin sheet) or plane strain (e.g., rolling of sheet metal). Reducing a Finite Element (FE) analysis from three to two dimensions in this way brings immediate computational benefits by greatly reducing the number of integration points to be considered for a given resolution of the deformation field.

When an anisotropic constitutive model is employed in the analysis, constraining the element formulation to plane stress or plane strain may allow for further simplifications, if certain assumptions about the symmetry of the material properties can be made. For example, in the case of rolling of sheet metal, the material is subjected to deformation that has two-fold rotational symmetry about the Transverse Direction (TD), so that the material will feature at least monoclinic symmetry of the macroscopic mechanical properties about that axis. Therefore, the shear strain components $\varepsilon_{\mathrm{RD-TD}}$ and $\varepsilon_{\mathrm{ND-TD}}$ should be negligible, and the deviatoric stresses $\sigma'_{\mathrm{RD-TD}}$ and $\sigma'_{\mathrm{ND-TD}}$ can be neglected, along with σ'_{TD}. In this case, the yield criterion ϕ is a function of only three deviatoric stress components $\phi(\sigma'_{\mathrm{RD}}, \sigma'_{\mathrm{ND}}, \sigma'_{\mathrm{RD-ND}})$.

[3] Slab analysis typically assumes homogeneous strains, perfect plasticity and rolling of thin sheet.

1.5. Anisotropic yield criteria and multiscale methods

Many commercial and research FEA packages used to simulate metal forming follow a displacement-driven approach, for which the onset of plastic yielding is conveniently described by a convex analytical function of the stress. The choice of such yield functions has been shown to affect prediction accuracy for many phenomena such as forming limits [56,57], springback [58] and earing profiles [59].

The first continuum mechanics theories of Tresca and von Mises were developed to explain experimentally observed macroscopic-level plasticity. They were found to be inaccurate for some sheet metals [60], inspiring the development of the first general anisotropic model for orthotropic material [61], whose experimental limitations [62] led to further refinements [63]. In recent years, a very large number of yield criteria have been developed for specific applications and materials, as surveyed, for example, by Banabic et al. [64], Barlat et al. [65], Chinesta and Cueto [66], Yoshida et al. [67], Bruschi et al. [68]. Many of these recent models are underpinned by the theory of representation of tensor functions [69,70], which provides a general framework for formulating convex anisotropic yield functions respecting the symmetry of material properties. In particular the method of linear transformation of the stress tensor, which is a special application of this theory (applied for example by Barlat et al. [71], Karafillis and Boyce [72]), has been shown to allow for an increase of the number of calibration parameters, and thus of the model's accuracy for some particular cases, without increasing the mechanical test data required [73].

A second direction in the development of yield functions is one seeking to account more directly for the link between the microstructure and the shape of the yield surface. Calculations of the theoretical upper bound of the yield surface for fcc materials [13] inspired researchers to propose new functions and develop methodologies to calibrate them using multi-scale models. These models account for the mechanisms of plastic slip, twinning, lattice rotation, and strain hardening [12, 74–82]. Within this approach, the concept of "hierarchical multiscale modelling" has evolved, where multiscale CP, Crystal Plasticity Finite Element Method (CPFEM) or Crystal Plasticity Fast Fourier Transform (CPFFT) models are used to calibrate a plastic potential function [83–85] or a traditional yield function[86,87] via "virtual mechanical tests". "Virtual mechanical testing" consists in employing multiscale models to simulate different mechanical tests to calibrate a yield function. Such tests include the simulation of deformations that are very difficult to carry out in experiments, but are valuable for the characterisation of material behaviour.

CP models operate with statistical information on the microstructure, typically the crystallographic texture and some aspect of the grain morphology, data that may be gathered through X-Ray Diffraction (XRD) and Orientation Imaging Microscopy (OIM) measurements. Examples of such models, in order of increasing computational cost, are the classic TBH model [13], the grain interaction [14,88–90], and self-consistent [91,92] models. Greater accuracy and the possibility to account for more physical phenomena is available at higher cost, in terms of computation and material characterisation, using the CPFEM [93] and CPFFT [94,95] approaches.

From the point of view of formulating and calibrating yield functions for practical applications, each of the two approaches outlined above have their own advantages: the first one aims to use a minimum of familiar mechanical tests for calibration, and benefits from extensive analysis and validation in the literature; the second one closely approximates the mechanical responses predicted by the chosen underlying models of the microstructure, which may account for many physical phenomena at meso- and microscopic scales, without the associated computational cost. The second approach is followed in this work: specifically it is a special case of the "FACET method" [83], which is based on a theory of plastic potentials [96], wherein a plastic potential function (a convex analytical expression) is (a) calibrated by using a multiscale model to find stresses for a set of strain rates, and (b) describes the full yield surface and its derivatives. It is assumed in this work that a strain-rate-driven CP model assumes the role of the "multiscale model". However, it should be pointed out that other types of material model may be substituted without modification as long as they provide a unique stress response for an imposed velocity gradient and satisfy the normality rule of plasticity theory.

2. Anisotropic 2D finite element model of asymmetric rolling

2.1. Crystal plasticity calibrated material law for 2D FEA

A conventional displacement-driven FEA software code requires a material constitutive model that can calculate the stress for a given increment of strain. To simulate a sheet metal forming problem, such a code must account, amongst other factors, for the typical anisotropy of the metal. In most engineering sheet metals, the plastic anisotropy can be deduced from the crystallographic texture using CP models. However, CP models are relatively computationally expensive in the context of FEA, in fact, so much so that the classic phenomenological models are still widely used in most commercial applications.

The FACET method was introduced by Van Houtte et al. [83] to allow CP models to be incorporated into FEA based multiscale models for engineering applications in a computationally efficient way. It specifies potential functions of either the stress $\boldsymbol{\sigma}$ or strain rate $\boldsymbol{D}$, which are usually denoted by $\phi(\boldsymbol{\sigma})$ and $\Psi(\boldsymbol{D})$ respectively. When an associated flow is assumed, such potential functions can be used to form yield functions. The functions $\Psi(\boldsymbol{D})$ and $\phi(\boldsymbol{\sigma})$ have certain properties in order to be suitable for use in FEA: (a) they are convex, (b) they are smooth and have analytic derivatives, (c) they can accurately reproduce the underlying CP model behaviour in the full deviatoric stress or strain rate space, including, e.g., Bauschinger effects. In the FACET method, the potential functions $\Psi(\boldsymbol{D})$ and $\phi(\boldsymbol{\sigma})$ are specified as homogeneous polynomials

of even order that always meet the above criteria; they are calibrated by finding the polynomial coefficients that reproduce the stress response of a polycrystal. In the current context, the stress responses are calculated by a CP model for a number of different strain rate modes, which is also known as virtual mechanical testing.

In this work, the virtual tests are defined by the choice of strain rates $\boldsymbol{D}$ used as input to the CP model, which provides the stress response $\boldsymbol{\sigma}$ as output. As there are no implicit symmetry constraints in the formulation of the potential function $\phi(\boldsymbol{\sigma})$ of the FACET method, a simple approach is to choose a set of strain rate modes that covers the strain rate space with approximately even density, but as a set features only triclinic symmetry. This avoids redundant virtual tests for a material with higher sample symmetry, such as the monoclinic symmetry resulting from the ASR process.

2.2. Facet yield function for 2D FEA

In this article, the FACET method is modified for application in a specific circumstance – namely the simplification of the expression for a stress space potential ϕ to be used as a conventional yield function $\phi^{\mathrm{s}}(\boldsymbol{\sigma})$ in a 2D FEA code. It may be noted that the potential function ϕ is expressed in deviatoric stress space, and is calibrated with the results of virtual tests that correspond to approximately evenly spaced points on the yield surface in the deviatoric stress space. Thus calibrated, it can be used both for plane stress or plane strain, as the two cases differ only in how the FE stress integration algorithm exploits the yield function. The superscript "s" in ϕ^{s} refers to the fact that ϕ^{s} describes the yield surface shape – this point will be returned to in section 2.6. Noting the use of the superscript k as an index of summation to avoid confusion with tensor component indices, the function $\phi^{\mathrm{s}}(\boldsymbol{\sigma})$ has the following form:

$$\phi^{\mathrm{s}}(s_q) = \left(s^* \sum_{k=1}^{m} \lambda^k (s_q d_q^k)^n \right)^{\frac{1}{n}} \tag{3}$$

$$m \geq 3, \quad n = 2l, \quad l \geq 1, \quad l, m, n \in \mathbb{N} \tag{4}$$

$$\lambda^k > 0, \quad \forall\, k \tag{5}$$

This expression is the nth root of a homogeneous polynomial of degree n – i.e. each of the terms is raised to the same power n (n is hereafter referred to as the *order* of the function ϕ^{s}). The term s^* is a scalar which normalises ϕ^{s} for some reference stress mode, as will be explained below. k is an index of summation. m is the total number of terms in the expression, which is related to the number of virtual tests used in the calibration; the λ^k are the adjustable weighting terms. The deviatoric stress term s_q is the running variable; the parameters $(d_q^1 \ldots d_q^k)$ have the meaning of deviatoric strain rates, and correspond to the strain rates chosen for the virtual mechanical tests. Both the input s_q and the parameters d_q^k are contracted forms of the deviatoric stress tensor $\boldsymbol{\sigma'}$ and deviatoric strain rate tensors $(\boldsymbol{D'}^1 \ldots \boldsymbol{D'}^k)$, where the index $q \in \{1, 2, 3\}$ also serves to emphasise the difference with the more usual A_{ij} notation for tensorial quantities.

The conditions of Eq. (4) are necessary for ϕ^{s} to be a closed surface,[4] and Eq. (5) ensures that this surface is convex, as proven by Van Houtte et al. [83]. The definition of the contraction for s_q (Eq. (6)) and d_q (Eq. (7)) is a special case of the contraction method proposed by Van Houtte et al. [83].

$$\boldsymbol{s} = \frac{1}{\sqrt{2}} \begin{pmatrix} \sigma'_{11} - \sigma'_{22} \\ \sqrt{3}(\sigma'_{11} + \sigma'_{22}) \\ 2\sigma'_{12} \end{pmatrix} \tag{6}$$

$$\boldsymbol{d} = \frac{1}{\sqrt{2}} \begin{pmatrix} \hat{D}'_{11} - \hat{D}'_{22} \\ \sqrt{3}\left(\hat{D}'_{11} + \hat{D}'_{22}\right) \\ 2\hat{D}'_{12} \end{pmatrix} \qquad \hat{D}'_q = \frac{\boldsymbol{D'}}{\left|\left|\boldsymbol{D'}\right|\right|_2} \tag{7}$$

The weight terms λ^k in Eq. (3) are calibrated for m stress and plastic strain rate pairs (s_q^k, d_q^k) that are obtained as the result of virtual mechanical tests. These virtual tests are carried out for a chosen number η of strain rate modes.

As mentioned above, ϕ^{s} is defined by Eq. (8) for some reference mode[5] of stress $\hat{\boldsymbol{s}}^*$. The conventional choice for a reference stress mode $\hat{\boldsymbol{s}}^*$ for sheet metal is one that corresponds to the uniaxial tensile test in the RD. In any case, once a choice is made for $\hat{\boldsymbol{s}}^*$, the value of s^* in Eq. (3) is determined per Eq. (8).

$$\text{definition: } \phi^{\mathrm{s}}(\hat{\boldsymbol{s}}^*) = 1 \quad \Rightarrow \quad s^* = \left(\sum_{k=1}^{m} \lambda^k (\hat{\boldsymbol{s}}_q^* d_q^k)^n \right)^{-1} \tag{8}$$

[4] More precisely, $m \geq N$ for an N-dimensional space; it is also necessary that at least N of the d_q have unique directions.

[5] A stress *mode* is a stress vector of the type in Eq. (6) that has unit length.

The first derivatives of ϕ^s, which will be required by the FEA code, can be derived using the chain rule, and are given in Eqs. (9) and (10).

$$\frac{\partial \phi^s}{\partial \sigma_{ij}} = \sum_{l=1}^{3} \frac{\partial \phi^s}{\partial s_l} \frac{\partial s_l}{\partial \sigma_{ij}} \tag{9}$$

$$\begin{aligned} \frac{\partial s_1}{\partial \sigma_{ij}} &= \frac{1}{\sqrt{2}} \begin{pmatrix} 1 & 0 & 0 \\ 0 & -1 & 0 \\ 0 & 0 & 0 \end{pmatrix} \quad \frac{\partial s_2}{\partial \sigma_{ij}} = \frac{1}{\sqrt{6}} \begin{pmatrix} 1 & 0 & 0 \\ 0 & 1 & 0 \\ 0 & 0 & -2 \end{pmatrix} \\ \frac{\partial s_3}{\partial \sigma_{ij}} &= \frac{1}{\sqrt{2}} \begin{pmatrix} 0 & 1 & 0 \\ 1 & 0 & 0 \\ 0 & 0 & 0 \end{pmatrix} \quad \frac{\partial \phi^s}{\partial s_l} = \frac{s^* \sum \lambda^k d_l^k (s_q d_q^k)^{n-1}}{\left(s^* \sum \lambda^k (s_q d_q^k)^n\right)^{\frac{n-1}{n}}} \end{aligned} \tag{10}$$

The anisotropy can be derived from the function ϕ^s in terms of the Lankford parameter r_θ or the contraction ratio q_θ. Eq. (11) defines the r_θ as a function of the angle θ of a tensile test sample with respect to RD; the contraction ratio q_θ is defined in Eq. (12). Eqs. (11), (13), and (14) can be used to calculate r_θ or q_θ from ϕ^s.

$$r_\theta = \frac{\mathrm{d}\varepsilon_{\text{width}}}{\mathrm{d}\varepsilon_{\text{thickness}}} \tag{11}$$

$$q_\theta = \frac{r_\theta}{1 + r_\theta} \tag{12}$$

$$\mathrm{d}\varepsilon_{ij} = d\lambda \frac{\partial \phi}{\partial \sigma_{ij}} \tag{13}$$

$$\begin{aligned} \mathrm{d}\varepsilon_{\text{length}} &= -2 \sin\theta \cos\theta \mathrm{d}\varepsilon_{12} + \cos^2\theta \mathrm{d}\varepsilon_{11} + \sin^2\theta \mathrm{d}\varepsilon_{22} \\ \mathrm{d}\varepsilon_{\text{width}} &= -2 \sin\theta \cos\theta \mathrm{d}\varepsilon_{12} + \cos^2\theta \mathrm{d}\varepsilon_{22} + \sin^2\theta \mathrm{d}\varepsilon_{11} \\ \mathrm{d}\varepsilon_{\text{thickness}} &= -(\mathrm{d}\varepsilon_{\text{length}} + \mathrm{d}\varepsilon_{\text{width}}) \end{aligned} \tag{14}$$

2.3. Calibration with virtual mechanical tests

First, the calibration problem is formulated as a standard matrix equation of the form $Ax = b$, which can be solved for x. Recalling that m is the number of terms in Eq. (3), and η is the number of chosen virtual tests, then in standard matrix form (i) the unknown x is an $m \times 1$ column matrix of the λ^k weighting values, (ii) $\boldsymbol{b}$ is an $m \times 1$ column matrix of ones, and (iii) A is an $\eta \times m$ matrix. Each row i and each column j in A is the evaluation of the jth term of ϕ^s for the ith calibrating stress $\boldsymbol{s}^i$:

$$\begin{pmatrix} (\boldsymbol{s}^1 \cdot \boldsymbol{d}^1)^n & \cdots & (\boldsymbol{s}^1 \cdot \boldsymbol{d}^m)^n \\ \vdots & & \vdots \\ (\boldsymbol{s}^\eta \cdot \boldsymbol{d}^1)^n & \cdots & (\boldsymbol{s}^\eta \cdot \boldsymbol{d}^m)^n \end{pmatrix} \begin{pmatrix} \lambda^1 \\ \vdots \\ \lambda^m \end{pmatrix} = \begin{pmatrix} 1 \\ \vdots \\ 1 \end{pmatrix} \tag{15}$$

Recalling the constraints of Eqs. (4) and (5), in particular that $\lambda^k \geq 0$, the Non Negative Least Squares (NNLS) method [97] can be used to solve for the column matrix of λ^k values in Eq. (15).

Employing Eq. (15) in its simplest form assumes an equal number η of calibrating stresses $\boldsymbol{s}$ and m of parameters $(\boldsymbol{d}, \lambda^k)$. Ideally, there would be no redundancy in the calibration data. Here "redundancy" can be understood in the sense that Eq. (15) is usually over-determined. In other words, more virtual tests than strictly necessary may have been carried out. There is no obvious way to determine *a priori* which set of parameters – i.e. strain rate directions $\boldsymbol{d}$, and their corresponding calibrating stresses $\boldsymbol{s}$ – are optimal. This is because the optimal choice of virtual tests depends on the morphology of the yield surface to be approximated, which is not known in advance.

Previous authors [87,84,83] have assumed an "equidistant grid", i.e. a set of stress mode or strain rate mode directions that, when considered as unit vectors, evenly cover the orientation space with some specified resolution. A large subset of the points in such grids have cubic symmetry, which would lead to many redundant virtual tests in materials with higher than triclinic sample symmetry. Thus, in the present case, the "spiral" algorithm presented by Saff and Kuijlaars [98] is adopted and used to generate η evenly spaced strain rates $\boldsymbol{d}$ with triclinic symmetry. Using the strain rates $\boldsymbol{d}^i$ as input, the ALAMEL CP model is used to carry out the virtual mechanical tests, which provides the stresses $\boldsymbol{s}^i$. The $\boldsymbol{d}^i$ and $\boldsymbol{s}^i$ are then substituted into Eq. (15), and the coefficients λ are found.

2.4. Texture measurements

The textures of two materials were measured to calibrate FACET yield functions for simulations of the deformation field and texture evolution during ASR. {111}, {200}, {220}, and {311} pole figures were measured on the mid-thickness RD-TD

Table 1
Common texture components and Miller indices for rolled materials with orthorhombic sample symmetry.

Name	Miller idx.	Euler angles†	Name	Miller idx.	Euler angles†
Copper	{112}⟨111⟩	(90°, 35°, 45°)	H	{001}⟨110⟩	(0°, 0°, 45°)
Brass	{011}⟨211⟩	(35°, 45°, 0°)	P‡	{011}⟨233⟩	(19°, 90°, 45°)
S3	{123}⟨634⟩	(59°, 36°, 63°)	F	{111}⟨211⟩	(90°, 54°, 45°)
Cube	{001}⟨100⟩	(0°, 0°, 0°)	E	{111}⟨110⟩	(60°, 54°, 45°)
Goss	{011}⟨100⟩	(0°, 45°, 0°)			

† Approximate Euler angles following the Bunge convention $(\varphi_1, \Phi, \varphi_2)$.
‡ Different definitions exist for the P component, e.g., {011}⟨122⟩, see [99,100]).

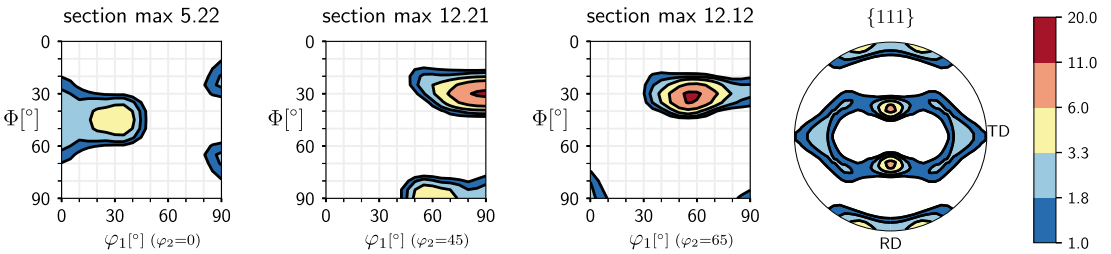

Fig. 1. Orientation Distribution Function (ODF) for AA1050-CR (cold rolled aluminium sheet) 1 mm sheet in as received condition: (left to right) $\varphi_2 = 0°, 45°$, and 65° ODF sections and {111} pole figure. The material has strong copper, brass, and S3 components.

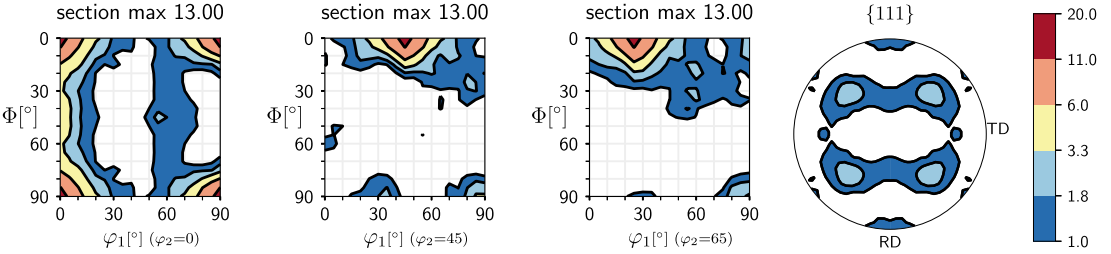

Fig. 2. ODF of AA6016-HR (hot rolled aluminium alloy sheet) 1.22-mm sheet in as received condition: (left to right) $\varphi_2 = 0°, 45°$, and 65° ODF sections and {111} pole figure. The material has a cube texture, with weak Goss and P components.

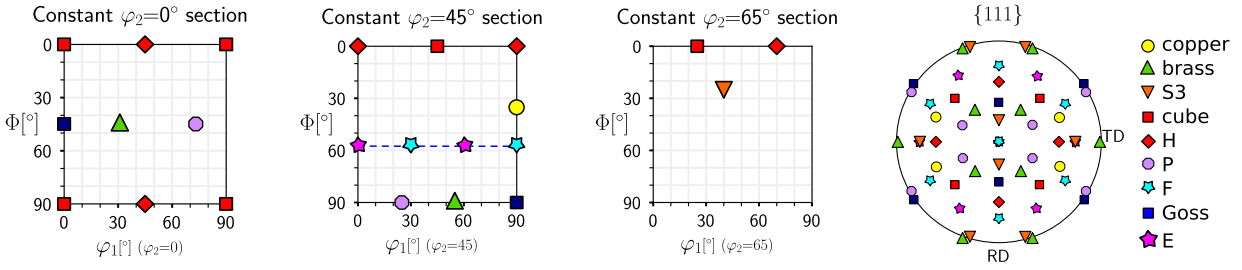

Fig. 3. Legend of texture components on the ODF assuming orthorhombic sample symmetry. The blue dashed line indicates the position of the γ fibre in the $\varphi_2 = 45°$ section.

plane with reflective XRD using a SIEMENS D500 goniometer. The device operates with a copper X-ray tube and a scintillation detector with Soller slits and a lithium fluoride monochromator.

Table 1 lists some of the standard texture components, and the corresponding positions in the Bunge Euler space conventionally used for material with orthorhombic sample symmetry are given in Fig. 3.

The 1XXX series aluminium alloys are technically pure-grade ones that are known to feature β fibre textures in the rolled condition, and strong cube textures when annealed after cold rolling. The ODF for a 1-mm-thick cold-rolled 1050 alloy, hereafter referred to as "AA1050-CR", is given in Fig. 1. As it is cold-rolled, this texture consists mainly of strong copper and S3 orientations, with a weaker brass component. The 6XXX series aluminium alloys typically have weaker rolling and annealing textures than the 1XXX series. Their textures feature the same components, with the exception of the *P* component, which is associated with Particle Stimulated Nucleation (PSN) [101]. The ODF of a hot-rolled 6016 alloy, referred to hereafter as "AA6016-HR", is shown in Fig. 2, where recrystallisation during interpass or batch annealing is expected to

cause the formation of a strong cube component. While, in general, the texture of any particular alloy is dependent on the composition and processing history, these two textures are somewhat typical examples of cold-rolled and hot-rolled sheet aluminium alloys [102,103].

2.5. Selecting parameters η, m, and n

As touched on above, it is not possible to prescribe optimal values for the number of virtual tests η, the order of the expression n, and the number of terms m that would be valid for all materials and all multiscale models. Optimal values depend on the characteristics of the yield surface being approximated, which is only known after some sufficient number of virtual tests are carried out.

In practise, however, one can determine parameter values that would be valid for a particular class of material, e.g., sheet aluminium, and a particular multiscale model, e.g., ALAMEL or TAYLOR FC, by studying the yield surface for one representative example. One carries out a large number N of virtual tests on the chosen example, and then calibrates FACET potential functions ϕ^s for a range of different values of η, n, and m. One then calculates an error value $\xi(\eta, n, m)$ for each calibrated function ϕ^s, which allows suitable values of η, n, and m to be found.

If the NNLS method is used to solve the calibration problem (Eq. (15)), then m can initially be chosen as $m^{\text{trial}} = \eta$. It is then typically found that some of the coefficients λ^i will be zero; in other words, the total number of terms m in the calibrated function ϕ^s with non-zero coefficients $\lambda^i \neq 0$ is less than m^{trial}. This means that, in practise, if we use the NNLS method and always assume $m^{\text{trial}} = \eta$, then m is not an independent parameter, but is some value $m < m^{\text{trial}}$, which is a result of the NNLS solution procedure. It then remains to find suitable values for η and n.

Two types of error variable are proposed here: the first of these is defined in Eqs. (16)–(18), and is referred to as the "strain rate matched stress error" ξ^σ (or "stress error" for short). It is the average of the Euclidean distances in deviatoric stress space between the reference stresses $\boldsymbol{\sigma}_i'^*$ (which are the direct response of the multiscale model to the input strain rates $\boldsymbol{D}_i^*$) and the corresponding FACET approximation stresses $\boldsymbol{\sigma}_i'$. The value for $\boldsymbol{\sigma}_i'$ is found by searching for the stress for which the derivative of ϕ is parallel to the strain rates $\boldsymbol{D}_i^*$, see Eq. (18):

$$\xi^\sigma = \frac{1}{N}\sum_{i=1}^{N} \frac{||\boldsymbol{\sigma}_i' - \boldsymbol{\sigma}_i'^*||}{||\boldsymbol{\sigma}_i'^*||} \tag{16}$$

$$\xi^\sigma_{\max} = \max\left(\frac{||\boldsymbol{\sigma}_i' - \boldsymbol{\sigma}_i'^*||}{||\boldsymbol{\sigma}_i'^*||}\right) \tag{17}$$

$$\text{with} \quad \alpha \left.\frac{\partial\phi}{\partial\boldsymbol{\sigma}}\right|_{\boldsymbol{\sigma}=\boldsymbol{\sigma}_i'^*} = \boldsymbol{D}^*, \quad \text{for some constant } \alpha \tag{18}$$

The second error variable is referred to as the "stress matched strain rate error" ξ^D (or "strain rate error" for short). It is based on the average of the cosines of the angles between the normalised strain rate vector of the reference $\hat{\boldsymbol{D}}_i^*$ and the normalised strain rate vector of the FACET expression, at the same stress $\boldsymbol{\sigma}_i' = \boldsymbol{\sigma}_i'^*$. It is defined in Eqs. (19)–(20):

$$\xi^D = \arccos\left\{\frac{1}{N}\sum_{i=1}^{N} \hat{\boldsymbol{D}}_i \cdot \left.\frac{\partial\phi}{\partial\boldsymbol{\sigma}}\right|_{\boldsymbol{\sigma}=\boldsymbol{\sigma}_i'}\right\} \tag{19}$$

$$\xi^D_{\max} = \arccos\left\{\max\left(\hat{\boldsymbol{D}}_i \cdot \left.\frac{\partial\phi}{\partial\boldsymbol{\sigma}}\right|_{\boldsymbol{\sigma}=\boldsymbol{\sigma}_i'}\right)\right\} \tag{20}$$

Fig. 4 plots the value of the stress error ξ^σ as a function of the number of virtual tests η, for the FACET functions ϕ^s with the order $n = 8$, for the AA1050-CR and AA6016-HR materials. Likewise Fig. 5 plots the value of the strain rate error ξ^D as a function of η. Here ξ^σ and ξ^D are calculated using a reference set of $N = 5000$ strain rate modes and corresponding stresses, derived directly from the TAYLOR FC CP model. Note that the TAYLOR FC model is used because, for a given texture, it typically predicts a more sharply featured yield surface, and more extreme variation in r values, which is more challenging to model with analytic expressions. It can be clearly seen that the error decreases rapidly with increasing η up to $\eta = 100$, after which little improvement in the calibrated expression is observed; this is true both for the averaged variables (ξ^σ, ξ^D) and those based on maxima ($\xi^\sigma_{\max}$, $\xi^D_{\max}$). All of the error variables display the same trend. As noted above, there are not in general $m = \eta$ terms in the calibrated solution, that in fact the number of terms m appears dependent on the sharpness of the texture, the available slip systems, the order n of the FACET expression and, to a lesser extent, on η itself. For example, with $n = 8$ and $\eta = 100$, for the materials in Figs. 4 and 5 it is found that $20 \leq m \leq 30$.

Next the value of the order n is determined by examining the effect of increasing n on ϕ. In principle, higher values of n allow a yield surface with very sharp edges and vertices to be modelled with greater fidelity. However, n cannot be

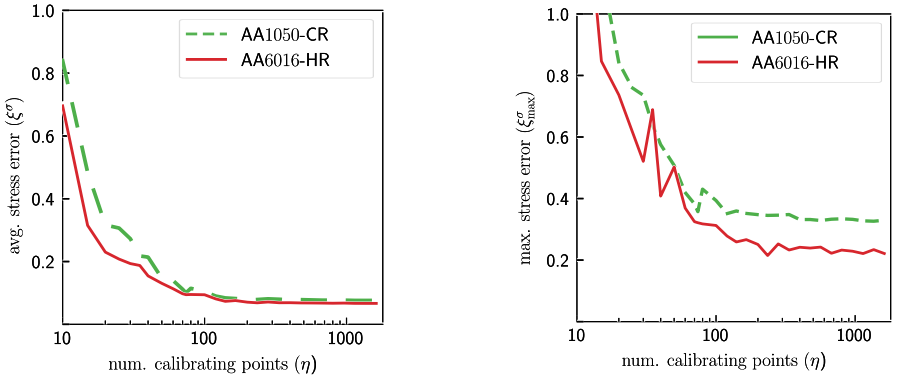

Fig. 4. Strain rate matched stress error ξ^σ for the calibrated FACET function ϕ^s (Eq. (3)) as a function of the number η of virtual tests used for calibration (Eq. (15)), for two textured sheet materials: (left) the average error values ξ^σ and (right) the maximum values $\xi^\sigma_{\max}$. The stress error decreases rapidly as η increases, up to $\eta = 100$, after which the error changes slowly. Note the logarithmic scale for the horizontal axis.

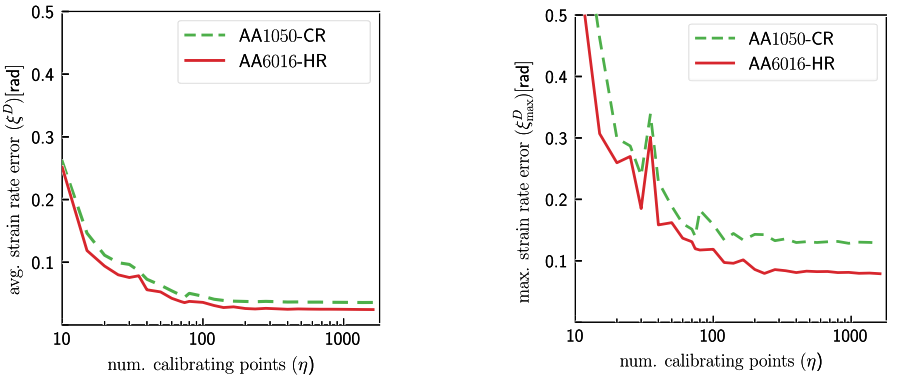

Fig. 5. Stress matched strain rate error ξ^D for the calibrated FACET function ϕ^s (Eq. (3)) as a function of the number η of virtual tests used for calibration (Eq. (15)), for two textured sheet materials: (left) the average ξ^D value and (right) the maximum $\xi^D_{\max}$ values. The error ξ^Ddecreases rapidly as η increases, up to $\eta = 100$, after which the error changes slowly. Note the logarithmic scale for the horizontal axis.

increased indefinitely as larger n requires larger number of terms m,[6] and may also introduce local curvatures in the yield surface which, though not breaking convexity, are not predicted by the CP model.

Taking the AA1050-CR material as an example, Fig. 6 (left) plots the variation of $\xi^D_{\max}$ with η for different orders n, while Fig. 6 (right) plots the number of terms m that are found in the calibrated function ϕ^η for the same data. Considering $n = 8$ as the reference, it appears that increasing the order above $n = 12$ reduces the error for $\eta > 100$ (Fig. 6, left). However, increasing the order above 16, e.g., for $n = 18$ causes the trend to reverse (the error begins to increase). These optimal values of n are higher than first reported by the authors of the FACET [83], but are in general agreement with recent findings [87]. In general, the higher the order n the greater the number of terms m, e.g., at a value $\eta = 200$ for the functions with $n \geq 14$ it is found that $50 \leq m \leq 60$ while $m = 27$ for $n = 8$ (Fig. 6, right). For all orders n, the number of terms m appears to increase slowly but indefinitely with η, despite there being no longer any decrease in error $\xi^D_{\max}$ for $\eta > 200$.

A more conventional analysis than the above would be to examine the yield loci for the calibrated functions ϕ^η, or plots based on the gradient of the functions ϕ such as those presented by Kuwabara et al. [104]. A section of the normalised σ_{11} σ_{22} yield locus and the corresponding gradient plot for the AA1050-CR material is given in Fig. 7, together with direct CP model values superimposed as open circles.[7] In this plot, it can be seen that $n = 12$ gives a yield locus and gradient plot that coincides with the CP results more closely than $n = 8$, but that the further improvement for $n = 16$ is very subtle.

Finally, it may be noted from the above that the calibration of the FACET potential function of Eq. (3), using the NNLS method and the spiral algorithm for selecting strain rate modes for virtual test, is stable. Which is to say that above a minimum number $\eta \geq 100$ of virtual tests and above a minimum order $n \geq 8$, the solution is (a) of good quality, and (b) does not change rapidly in quality, even with changes in η and n.

In summary, for the textured aluminium materials examined here, it appears that a reduced space FACET expression can be accurately calibrated using $\eta = 200$ virtual tests. The potential function ϕ should have order $n = 12$, which results in

[6] The computational cost is proportional to m, and minimising m is particularly desirable in an explicit FEA context.

[7] Note that these superimposed CP values were not used in the calibration, but are calculated separately for the purpose of comparison.

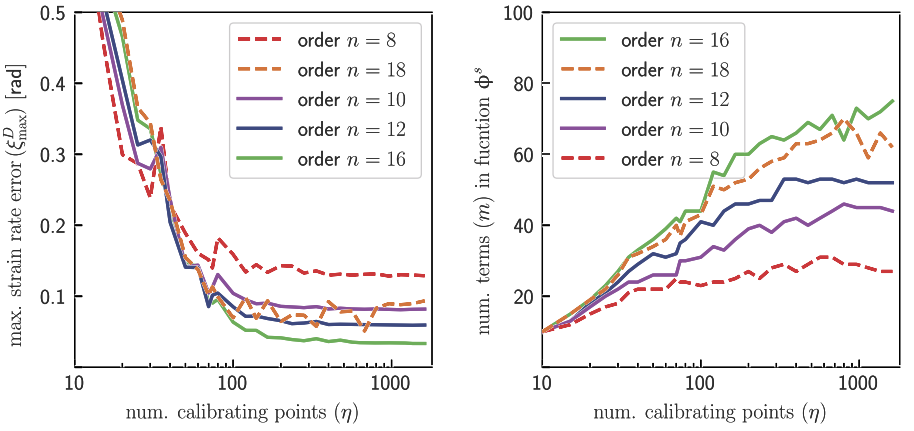

Fig. 6. Affect of order n on the FACET function ϕ^s (Eq. (3)) for the AA1050-CR material. (Left) Affect of order n on the strain rate error ξ^D as a function of the number of points η used to calibrate ϕ^s (Eq. (3)) – error reduces rapidly as η increases, up to $\eta = 100$, but decreases very slowly thereafter; (right) affect of order n on the number terms m in the calibrated FACET function ϕ^s (i.e. the number of terms with non-zero coefficients $\lambda^i \neq 0$ after solving Eq. (15)), as a function of the number of points η used in the calibration – m appears to increase indefinitely with η, but at a slow rate; note the use of a log scale for η in both cases.

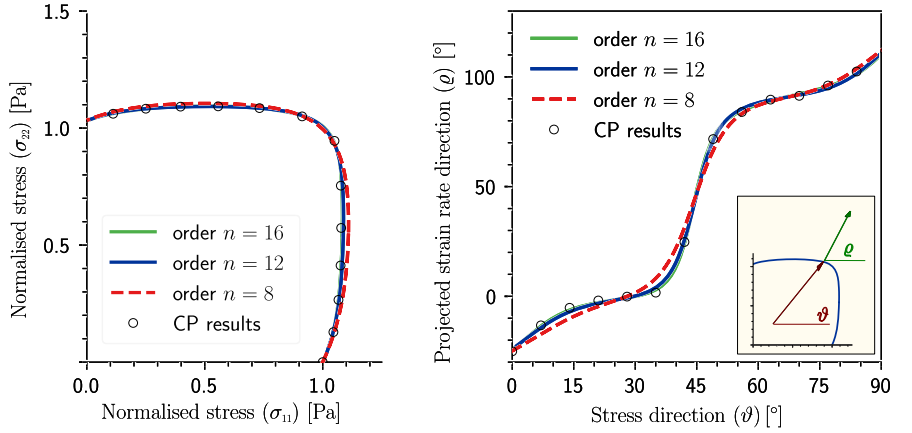

Fig. 7. A section of the normalised yield locus (left) and gradient plot (right) of a FACET function ϕ^s calibrated for AA1050-CR (cold rolled aluminium sheet) with $\eta = 200$ virtual tests, as a function of the order n. (Left) A section of the σ_{11}–σ_{22} yield locus for three values of the order (n); (right) the gradient plot for this yield locus section. The inset image illustrates the meaning of the angles ϑ and ϱ; more information on this type of plot is given in [104].

$m \approx 40$ terms. Higher-order expressions do not appear to require more calibration stresses, i.e. $\eta = 200$ is sufficient in all cases. Increasing the order above $n = 16$ reduces the accuracy of the calibration.

2.6. Plastic corrector stress increment

An infinitesimal increment of strain $\mathrm{d}\boldsymbol{\varepsilon}$ can be additively decomposed into elastic and plastic parts $\mathrm{d}\boldsymbol{\varepsilon} = \mathrm{d}\boldsymbol{\varepsilon}^{\mathrm{e}} + \mathrm{d}\boldsymbol{\varepsilon}^{\mathrm{p}}$. The increment of stress $\mathrm{d}\boldsymbol{\sigma}$ for an isotropic linear elastic material can be found from the elastic part of the strain $\mathrm{d}\boldsymbol{\varepsilon}^{\mathrm{e}}$ using the elastic stiffness tensor $\boldsymbol{C}$ of Hooke's law (Eq. (21)) as Eq. (22):

$$\boldsymbol{\sigma} = \boldsymbol{C} : \boldsymbol{\varepsilon}^{\mathrm{e}} \tag{21}$$

$$\mathrm{d}\boldsymbol{\sigma} = \boldsymbol{C} : \mathrm{d}\boldsymbol{\varepsilon}^{\mathrm{e}} = \boldsymbol{C} : \mathrm{d}\boldsymbol{\varepsilon} - \boldsymbol{C} : \mathrm{d}\boldsymbol{\varepsilon}^{\mathrm{p}} \tag{22}$$

The stress increment $\mathrm{d}\boldsymbol{\sigma}$ can be thus viewed as being composed of two parts, per Eq. (23): (a) a hypothetical "trial" or "predictor" increment $\mathrm{d}\boldsymbol{\sigma}^{\mathrm{tr}} = \boldsymbol{C} : \mathrm{d}\boldsymbol{\varepsilon}^{\mathrm{e}}$, which represents the stress increment if the strain increment were to be fully elastic, and (b) a plastic "corrector" increment $\mathrm{d}\boldsymbol{\sigma}^{\mathrm{p}} = \boldsymbol{C} : \mathrm{d}\boldsymbol{\varepsilon}^{\mathrm{p}}$, which corrects the trial value to account for plasticity that occurs during the increment.

$$\mathrm{d}\boldsymbol{\sigma} = \mathrm{d}\boldsymbol{\sigma}^{\mathrm{tr}} - \mathrm{d}\boldsymbol{\sigma}^{\mathrm{p}} \tag{23}$$

If a yield criterion ϕ is a function of the stress $\boldsymbol{\sigma}$ and the material state (represented by a vector of variables $\boldsymbol{\kappa}$), then from the onset of plasticity the following is required to hold:

$$\phi(\boldsymbol{\sigma}, \boldsymbol{\kappa}) = 0 \tag{24}$$

This constraint is referred to as "the consistency condition", and can be interpreted to mean that the stress must remain on the surface represented by Eq. (24) during plasticity. This constraint also applies for increments of the stress $\mathrm{d}\boldsymbol{\sigma}$ or changes in the material properties $\mathrm{d}\boldsymbol{\kappa}$, e.g., due to strain hardening, so that the following holds:

$$\phi(\boldsymbol{\sigma} + \mathrm{d}\boldsymbol{\sigma}, \boldsymbol{\kappa} + \mathrm{d}\boldsymbol{\kappa}) = \phi(\boldsymbol{\sigma}, \boldsymbol{\kappa}) + \frac{\partial \phi}{\partial \boldsymbol{\sigma}} : \mathrm{d}\boldsymbol{\sigma} + \frac{\partial \phi}{\partial \boldsymbol{\kappa}} : \mathrm{d}\boldsymbol{\kappa} = 0 \tag{25}$$

If the partial derivatives are held constant for the small but finite increments $\Delta\boldsymbol{\sigma}$ and $\Delta\boldsymbol{\kappa}$, and evaluated at some stress $\boldsymbol{\sigma}^{(t+\delta t)}$ and state $\boldsymbol{\kappa}^{(t+\delta t)}$ at the time $t+\delta t$ during the increment, then with reference to Eq. (24) Eq. (25) may be approximated as:

$$\phi(\boldsymbol{\sigma} + \mathrm{d}\boldsymbol{\sigma}, \boldsymbol{\kappa} + \mathrm{d}\boldsymbol{\kappa}) \approx \Delta\boldsymbol{\sigma} : \left.\frac{\partial \phi}{\partial \boldsymbol{\sigma}}\right|_{\boldsymbol{\sigma}^{(t+\delta t)}} + \Delta\boldsymbol{\kappa} : \left.\frac{\partial \phi}{\partial \boldsymbol{\kappa}}\right|_{\boldsymbol{\kappa}^{(t+\delta t)}} = 0 \tag{26}$$

In a forward Euler procedure, the derivatives of Eq. (26) would be evaluated at the beginning of the increment (i.e. at $\boldsymbol{\sigma} = \boldsymbol{\sigma}^{(t)}$, $\boldsymbol{\kappa} = \boldsymbol{\kappa}^{(t)}$), but the stress would in general drift outside of the yield surface during successive increments due to an accumulation of approximation errors. In a backward Euler procedure, the derivatives would be evaluated at the end of the increment (i.e. at $\boldsymbol{\sigma} = \boldsymbol{\sigma}^{(t+\Delta t)}$, $\boldsymbol{\kappa} = \boldsymbol{\kappa}^{(t+\Delta t)}$), so that the consistency condition would be fulfilled with a specifiable accuracy at the end of the increment, and drift would be avoided. In general a backward Euler procedure requires iteration as the derivative at the end of the increment is typically unknown.[8] However, in the context of an explicit FEA procedure, it is assumed that the small magnitude of the increments permit derivatives evaluated at some intermediate moment $(t+\delta t)$ within the increment to be good approximations of their value at the end of the increment $(t+\Delta t)$, so that there is no need for iterative refinement. In the current case, derivatives of ϕ with respect to the stress are evaluated at the point on the yield surface that is intersected by a line along the direction of trial stress $\boldsymbol{\sigma}^{\mathrm{tr}}$, which is considered a suitable approximation. Derivatives with respect to the material state $\boldsymbol{\kappa}$ are evaluated at the beginning of the increment.

It is assumed in ABAQUS© that the strain rate mode is constant during the increment,[9] and it is likewise here assumed that the plastic strain mode is constant during the increment. Assuming that the yield function and the plastic potential are identical,[10] the increment of plastic strain $\Delta\boldsymbol{\varepsilon}^{\mathbf{p}}$ can be related to the function ϕ with a scalar $\mathrm{d}\lambda$ by means of the associated flow rule of plasticity theory:

$$\Delta\boldsymbol{\varepsilon}^{\mathbf{p}} = \int_{t}^{t+\Delta t} \mathrm{d}\boldsymbol{\varepsilon}^{\mathrm{p}} = \int \frac{\partial \phi}{\partial \boldsymbol{\sigma}} \mathrm{d}\lambda \approx \Delta\lambda \left.\frac{\partial \phi}{\partial \boldsymbol{\sigma}}\right|_{\boldsymbol{\sigma}^{(t+\delta t)}} \tag{27}$$

The associated flow rule implies that the plastic strain rate direction (or the direction of a small increment of plastic strain $\Delta\boldsymbol{\varepsilon}^{\mathbf{p}}$) at yield is determined by the normal to the yield surface represented by a contour $\phi = \text{constant}$. As explained above, the derivatives of ϕ, and thus $\Delta\boldsymbol{\varepsilon}^{\mathbf{p}}$, are evaluated at the stress point on the yield surface that is intersected by a line along the direction of trial stress $\boldsymbol{\sigma}^{\mathrm{tr}}$, which approximates the stress point at the end of the increment. The increment $\Delta\lambda$ of the variable $\mathrm{d}\lambda$, sometimes called the "plastic multiplier", is a scalar measure of the magnitude of the increment of plastic strain. As with the consistency condition, the derivative in Eq. (27) is assumed constant and evaluated at the same intermediate point within the increment (i.e. $\boldsymbol{\sigma}^{(t+\delta t)} \parallel \boldsymbol{\sigma}^{\mathrm{tr}}$).

Assuming the yield surface does not change shape during the increment, but only scales isotropically as a function of the state variables $\boldsymbol{\kappa}$, the function ϕ can be separated into a function $\phi^{s}(\boldsymbol{\sigma})$ describing the surface shape and a function $\phi^{h}(\boldsymbol{\kappa}) = \sigma^{y}(\boldsymbol{\kappa})$ describing the scaling, where σ^{y} is the equivalent yield stress:

$$\phi(\boldsymbol{\sigma}, \boldsymbol{\kappa}) = \phi^{\mathrm{s}}(\boldsymbol{\sigma}) - \sigma^{y}(\boldsymbol{\kappa}) = 0 \tag{28}$$

This assumption allows separation of the variables in Eq. (26) so that it can be written:

$$\Delta\boldsymbol{\sigma} : \frac{\partial \phi^{\mathrm{s}}}{\partial \boldsymbol{\sigma}} - \Delta\boldsymbol{\kappa} : \frac{\partial \sigma^{y}}{\partial \boldsymbol{\kappa}} = 0 \tag{29}$$

It is then assumed that the evolution of the mechanical properties of the material due to plastic strain, i.e. the change in the yield stress σ^{y}, can be completely accounted for by a single variable $\boldsymbol{\kappa} = \epsilon^{\mathrm{eq}}$ and its increment $\Delta\boldsymbol{\kappa} = \Delta\epsilon^{\mathrm{eq}}$, representing a scalar measure of the magnitude of the plastic strain:

[8] An exception to this would be if the von Mises criterion were assumed for ϕ.

[9] "*We assume that the stretch at any time during the increment has the same principal directions as the total increment of stretch… This assumption might be questionable if the increments are very large, but it is consistent with the levels of approximation used in the integration of the inelastic constitutive model*" [105].

[10] In other words, they are both represented by the same continuous function ϕ with continuous first derivatives.

$$\begin{aligned}\sigma^{y}(\boldsymbol{\kappa}+\Delta\boldsymbol{\kappa}) &= \sigma^{y}\left(\epsilon^{\mathrm{eq}}+\Delta\epsilon^{\mathrm{eq}}\right)\\ &\approx \sigma^{y}\left(\epsilon^{\mathrm{eq}}\right)+\Delta\epsilon^{\mathrm{eq}}\left.\frac{\mathrm{d}\sigma^{y}}{\mathrm{d}\epsilon^{\mathrm{eq}}}\right|_{\boldsymbol{\sigma}=\boldsymbol{\sigma}^{(t)}}\end{aligned} \tag{30}$$

The scalar ϵ^{eq}, referred to hereafter as the "accumulated plastic strain", is the sum of all increments of equivalent plastic strain $\Delta\epsilon^{\mathrm{eq}}$ since the beginning of plastic deformation. The single-variable derivative in Eq. (30) can be interpreted as the slope of the equivalent stress vs. equivalent strain curve defining the isotropic hardening, and is evaluated at the start of the increment, qualifying Eq. (30) as a forward Euler approximation. The increment $\Delta\epsilon^{\mathrm{eq}}$ is a work-equivalent plastic strain defined in terms of the equivalent stress σ^{eq}, the deviatoric stress $\boldsymbol{\sigma'}$, and the increment of plastic strain $\Delta\boldsymbol{\varepsilon}^{\mathbf{p}}$ (with reference to Eq. (27)):

$$\sigma^{\mathrm{eq}}\cdot\Delta\epsilon^{\mathrm{eq}} = \boldsymbol{\sigma'}:\Delta\boldsymbol{\varepsilon}^{\mathbf{p}} \tag{31}$$

$$\Delta\epsilon^{\mathrm{eq}} = \frac{\boldsymbol{\sigma'}:\Delta\boldsymbol{\varepsilon}^{\mathbf{p}}}{\sigma^{\mathrm{eq}}} = \Delta\lambda\left(\frac{\boldsymbol{\sigma'}:\dfrac{\partial\phi^{s}}{\partial\boldsymbol{\sigma}}}{\phi^{s}(\boldsymbol{\sigma})}\right) \tag{32}$$

The consistency condition of Eq. (26) can then be rewritten as:

$$\frac{\partial\phi^{s}}{\partial\boldsymbol{\sigma}}:\Delta\boldsymbol{\sigma} = \frac{\mathrm{d}\sigma^{y}}{\mathrm{d}\epsilon^{\mathrm{eq}}}\Delta\epsilon^{\mathrm{eq}} = \Delta\lambda\frac{\mathrm{d}\sigma^{y}}{\mathrm{d}\epsilon^{\mathrm{eq}}}\left(\frac{\boldsymbol{\sigma'}:\dfrac{\partial\phi^{s}}{\partial\boldsymbol{\sigma}}}{\phi^{s}(\boldsymbol{\sigma})}\right) \tag{33}$$

Rewriting Eq. (22) in incremental form, and using the definition of $\Delta\epsilon^{\mathrm{eq}}$ in Eq. (31), one has:

$$\Delta\boldsymbol{\sigma} = \boldsymbol{C}:\left(\Delta\boldsymbol{\varepsilon}-\Delta\lambda\frac{\partial\phi^{s}}{\partial\boldsymbol{\sigma}}\right) \tag{34}$$

Substituting $\Delta\boldsymbol{\sigma}$ of Eq. (34) into Eq. (33) gives:

$$\frac{\partial\phi^{s}}{\partial\boldsymbol{\sigma}}:\boldsymbol{C}:\left(\Delta\boldsymbol{\varepsilon}-\Delta\lambda\frac{\partial\phi^{s}}{\partial\boldsymbol{\sigma}}\right) = \Delta\lambda\frac{\mathrm{d}\sigma^{y}}{\mathrm{d}\epsilon^{\mathrm{eq}}}\left(\frac{\boldsymbol{\sigma'}:\dfrac{\partial\phi^{s}}{\partial\boldsymbol{\sigma}}}{\phi^{s}(\boldsymbol{\sigma})}\right) \tag{35}$$

Rearranging Eq. (35) allows the unknown $\Delta\lambda$ to be written in terms of known quantities:

$$\Delta\lambda = \frac{\dfrac{\partial\phi^{s}}{\partial\boldsymbol{\sigma}}:\boldsymbol{C}:\Delta\boldsymbol{\varepsilon}}{\dfrac{\partial\phi^{s}}{\partial\boldsymbol{\sigma}}:\boldsymbol{C}:\dfrac{\partial\phi^{s}}{\partial\boldsymbol{\sigma}}+\dfrac{\mathrm{d}\sigma^{y}}{\mathrm{d}\epsilon^{\mathrm{eq}}}\left(\dfrac{\boldsymbol{\sigma'}:\dfrac{\partial\phi^{s}}{\partial\boldsymbol{\sigma}}}{\phi^{s}(\boldsymbol{\sigma})}\right)} \tag{36}$$

If $\boldsymbol{A}$ and $\boldsymbol{B}$ are two symmetric deviatoric tensors, and $\boldsymbol{C}$ is the stiffness tensor for an isotropic elastic material, the expression of Eq. (37) can be written (where μ is Lamé's second parameter):

$$\boldsymbol{A}':\boldsymbol{C}:\boldsymbol{B}' = 2\mu\boldsymbol{A}':\boldsymbol{B}' \tag{37}$$

As the tensors appearing in tensor products with $\boldsymbol{C}$ are deviatoric, Eq. (37) can be used to simplify Eq. (36) further:

$$\frac{\partial\phi^{s}}{\partial\boldsymbol{\sigma}}:\boldsymbol{C}:\Delta\boldsymbol{\varepsilon} = 2\mu\frac{\partial\phi^{s}}{\partial\boldsymbol{\sigma}}:\Delta\boldsymbol{\varepsilon} \tag{38}$$

$$\frac{\partial\phi^{s}}{\partial\boldsymbol{\sigma}}:\boldsymbol{C}:\frac{\partial\phi^{s}}{\partial\boldsymbol{\sigma}} = 2\mu\frac{\partial\phi^{s}}{\partial\boldsymbol{\sigma}}:\frac{\partial\phi^{s}}{\partial\boldsymbol{\sigma}} = 2\mu\left\|\frac{\partial\phi^{s}}{\partial\boldsymbol{\sigma}}\right\|^{2} \tag{39}$$

$$\Delta\lambda = \frac{2\mu\dfrac{\partial\phi^{s}}{\partial\boldsymbol{\sigma}}:\Delta\boldsymbol{\varepsilon}}{2\mu\left\|\dfrac{\partial\phi^{s}}{\partial\boldsymbol{\sigma}}\right\|^{2}+\dfrac{\mathrm{d}\sigma^{y}}{\mathrm{d}\epsilon^{\mathrm{eq}}}\left(\dfrac{\boldsymbol{\sigma'}:\dfrac{\partial\phi^{s}}{\partial\boldsymbol{\sigma}}}{\phi^{s}(\boldsymbol{\sigma})}\right)} \tag{40}$$

$$\Delta\boldsymbol{\sigma}^{\mathbf{p}} = \boldsymbol{C}:\Delta\boldsymbol{\varepsilon}^{\mathbf{p}} = 2\mu\Delta\lambda\frac{\partial\phi^{s}}{\partial\boldsymbol{\sigma}} \tag{41}$$

2.7. Stress integration algorithm

The procedure outlined below is used to implement a stress integration algorithm for a linear isotropic elastic/anisotropic plastic material in the context of a 2D FE analysis. This integration algorithm is implemented for plane strain according to this schematic as a set of FORTRAN subroutines and modules. The meaning of each symbol and variable is defined in the previous section 2.6.

Algorithm 1: Predictor–corrector stress integration algorithm for plane strain.

Data: strain increment $\Delta\boldsymbol{\varepsilon}$, and current state $(\boldsymbol{\sigma}^{(t)}, \boldsymbol{\varepsilon}^{(t)}, \epsilon^{\mathrm{eq}(t)})$ at time t
Result: updated state $(\boldsymbol{\sigma}^{(t+\Delta t)}, \epsilon^{\mathrm{eq}(t+\Delta t)})$ at time $(t+\Delta t)$

begin
- let $\boldsymbol{\sigma}^{\mathrm{tr}} = \boldsymbol{\sigma}^{(t)} + \boldsymbol{C} : \Delta\boldsymbol{\varepsilon}$; ▷ trial stress
- Evaluate $\phi = \phi^s(\boldsymbol{\sigma}^{\mathrm{tr}}) - \sigma^y(\epsilon^{\mathrm{eq}})$;
- **if** $\phi \leq 0$ **then**
  - $\boldsymbol{\sigma}^{(t+\Delta t)} = \boldsymbol{\sigma}^{\mathrm{tr}}$; ▷ stress = trial stress
  - $\epsilon^{\mathrm{eq}(t+\Delta t)} = \epsilon^{\mathrm{eq}(t)}$; ▷ no hardening
- **else**
  - Evaluate $\dfrac{\mathrm{d}\sigma^y}{\mathrm{d}\epsilon^{\mathrm{eq}}}$ at $\boldsymbol{\sigma}^{(t)}$; ▷ Slope of hardening curve
  - Evaluate $\dfrac{\partial\phi^s}{\partial\boldsymbol{\sigma}}$ at yield surf. in the direction of $\boldsymbol{\sigma}^{\mathrm{tr}}$;
  - Evaluate $\Delta\lambda$ via Eq. (40) ;
  - Evaluate $\Delta\boldsymbol{\sigma}^p$ via Eq. (41) ;
  - Evaluate $\Delta\epsilon^{\mathrm{eq}}$ via Eq. (32) ;
  - $\boldsymbol{\sigma}^{(t+\Delta t)} = \boldsymbol{\sigma}^{\mathrm{tr}} - \Delta\boldsymbol{\sigma}^p$;
  - $\epsilon^{\mathrm{eq}(t+\Delta t)} = \epsilon^{\mathrm{eq}(t)} + \Delta\epsilon^{\mathrm{eq}}$; ▷ update of material state
- **return** $\boldsymbol{\sigma}^{(t+\Delta t)}, \epsilon^{\mathrm{eq}(t+\Delta t)}$

This procedure describes the solution to the constitutive model for one increment of an explicit FE solution procedure. It requires one evaluation of the yield function ϕ^s for every increment for each integration point in the model to check if plasticity has occurred; for each integration point where plasticity indeed occurs, the derivative of ϕ^s with respect to stress is also required, along with the derivative of the equivalent stress/equivalent strain curve.

2.8. Parametric model of asymmetric rolling

A parametric model of the ASR process was designed to study the evolution of texture and texture gradients in ASR. This model is discussed in detail in an earlier work [106], where only isotropic plasticity was assumed. In the present case, this parametric model is extended with a user material subroutine to use the anisotropic FACET model of Eq. (3), and is employed as follows: (a) three levels of rolling pass reduction are considered, $\rho_{\mathrm{rr}} \in \{20\%, 30\%, 40\%\}$; (b) four values of the ratio of upper to lower roll ratio are modelled, $\rho_{\mathrm{ul}} \in \{1.0, 1.25, 1.5, 1.75\}$; (c) three values of the ratio of roll-radius-to-sheet-thickness are used, $\rho_{\mathrm{ut}} \in \{10, 20, 30\}$; (d) the python Application Programming Interface (API) and the explicit solver of the FEA package ABAQUS© is used to obtain the deformation field for every combination of the above parameters; (e) the rolls are assumed to be rigid and the deformable sheet is modelled with first-order plane strain elements, (f) between ten and twenty element layers were used in the sheet thickness, depending on the ratio of upper to lower roll radii ρ_{ul}, giving meshes with 1000 to 2500 elements; (g) contact is modelled with a linear pressure/overclosure relationship for normal stresses and a Coulomb friction coefficient of $\mu = 0.2$ for tangential stresses; (h) strain hardening is modelled with the power law of Eq. (42) with $K = 692$ MPa, $n = 0.275$ and $\varepsilon_0 = 0.01$, considered representative of the 6XXX alloys; (i) the FACET model is used as yield criterion, and is calibrated with virtual mechanical tests using the ALAMEL model for each of the two textures shown in Fig. 1 and Fig. 2; (j) nodal positions of elements in a steady-state "zone of interest" spanning the thickness of the sheet are exported and used to calculate velocity gradient $\boldsymbol{L}(t, y)$ as a function of time t and position in the sheet thickness y; (k) $\boldsymbol{L}(t, y)$ is input to the ALAMEL CP model to calculate texture evolution.

$$\sigma^{\mathrm{eq}} = K\,(\varepsilon_0 + \boldsymbol{\varepsilon})^n \tag{42}$$

3. Results

A parametric study of ASR is carried out using FEA with the new FACET model as a yield criterion (see section 2.2) to study the effect of anisotropy on the evolution of texture and texture gradients. As described in section 2.8, the deformation field in ASR was calculated for three levels of rolling pass reduction, ρ_{rr}, four values of roll ratio ρ_{ul}, and three values of the ratio of roll-radius-to-sheet-thickness ρ_{ut}. The FACET model is calibrated with virtual mechanical tests using the ALAMEL model for each of the two textures shown in Fig. 1 and Fig. 2. These textures are considered as textures representative of sheet

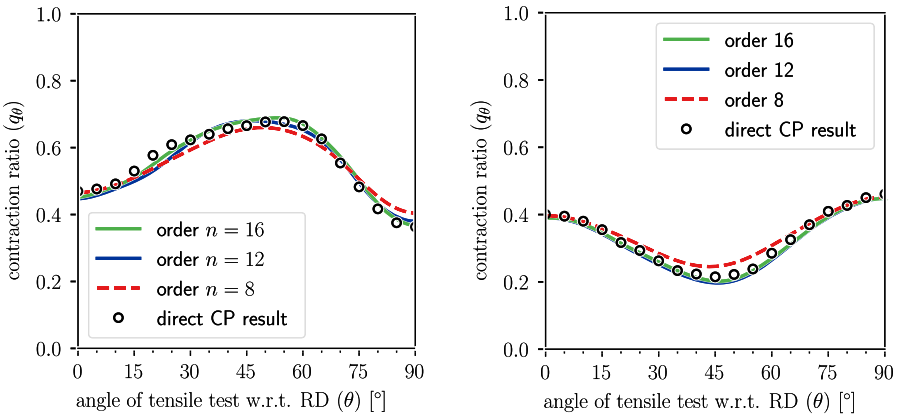

Fig. 8. Contraction ratio (q_θ) values from FACET functions ϕ^s for various orders (n) compared to direct CP results: (left) AA1050-CR (cold rolled aluminium sheet), (right) AA6016-HR (hot rolled aluminium alloy sheet).

aluminium alloys close to the start and the end of the cold rolling process. In other words, the texture of the AA6016-HR material features the mixed cube and β fibre typical for the early stages of cold rolling, while the AA1050-CR material features the strong β fibre texture typical for the later stages.

Firstly, results confirming the ability of the new FACET model to reproduce the anisotropic material properties predicted by the ALAMEL CP are presented. The results of the parametric study are then given, and the relevance to texture control in ASR is discussed.

3.1. Quality of anisotropy approximation by FACET

The anisotropy of the two textured materials displayed in Fig. 1 and Fig. 2 is assessed by calculating the parameters r_θ and q_θ (defined in Eqs. (11) and (12)) as a function of the angle of the tensile direction θ with respect to the sheet RD. The anisotropy parameters are plotted in Fig. 8, where the open circles represent the anisotropy calculated directly from the texture by the CP model, while the continuous lines represent the anisotropy values calculated from the derivatives of the corresponding calibrated FACET function, found using Eqs. (11), (13) and (14).

It can be observed that these two materials (a) have clearly different anisotropy due to their different textures, and that (b) the FACET model closely reproduces the anisotropy of the underlying CP model behaviour. The effect of the choice of order n for the FACET function is also shown in Fig. 8. Increasing n improves the agreement between the direct CP results and the FACET derived values, though little further improvement is seen for $n > 12$. In the simulations that follow, the order $n = 12$ is assumed.

3.2. Effect of anisotropy on texture evolution

The goal of the present section is to examine the influence of anisotropy in a range of configurations of the ASR process. In essence, it is a theoretical exploration that separates the anisotropy from its origin, i.e. the inhomogeneous and evolving texture of the material, so that it can be manipulated as an independent process parameter. In the same vein, an additional simplification is made so that texture evolution occurring during the process does not influence the deformation field. If these idealisations were not made, one would be faced with comparing the effects of different initial anisotropies on processes that perforce have different starting textures, and different paths of evolution – in other words not comparing like with like.

For the purpose of the exercise, it is therefore necessary to assume that some single texture can be usefully considered representative of sheet aluminium alloys undergoing cold rolling – to this end the texture of the AA6016-HR material is adopted (see section 2.4).

Fig. 9 presents box plots of evolution of the two most important texture components, namely the γ and β fibres, for all configurations of the ASR simulated in the parametric study. The evolution assuming the anisotropy of AA1050-CR is plotted on the left, while the results assuming the anisotropy of AA6016-HR are shown on the right. The upper, lower and middle horizontal lines of the boxes represent the upper and lower quartiles, and the median, respectively, of the relevant data, while the whiskers represent minimum and maximum values, excluding outliers; outliers are defined as those values greater than 1.5 times the upper or lower quartiles. The dotted and dashed lines indicate the volume fractions of the γ and β fibres in the material before rolling.

For both types of material, it can be seen that the volume fraction of the β fibre is reduced and that of the γ fibre is increased as the asymmetry of the process increases (the asymmetry is expressed here in terms of the roll radius ratio ρ_{ul}). This trend agrees with earlier results obtained with an isotropic material model [106]. However, the influence of the

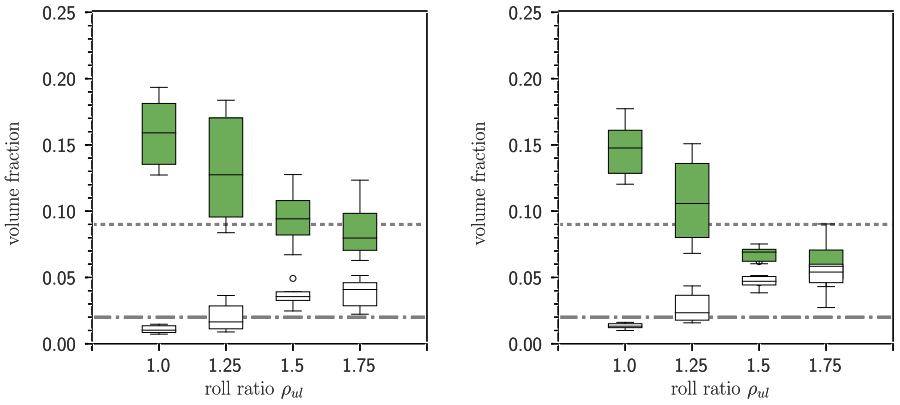

Fig. 9. Volume fractions of the γ and β texture components after ASR, with the same starting texture. The shaded boxes represent values for the γ fibre, and the unshaded boxes represent β fibre. (Left) results of texture evolution due to ASR assuming the anisotropy derived the texture of the alumjurijlong (Fig. 2) and (right) the result assuming the cold rolling texture of Fig. 1. The dotted and dashed lines indicate the volume fractions of the γ and β fibres in the material before rolling.

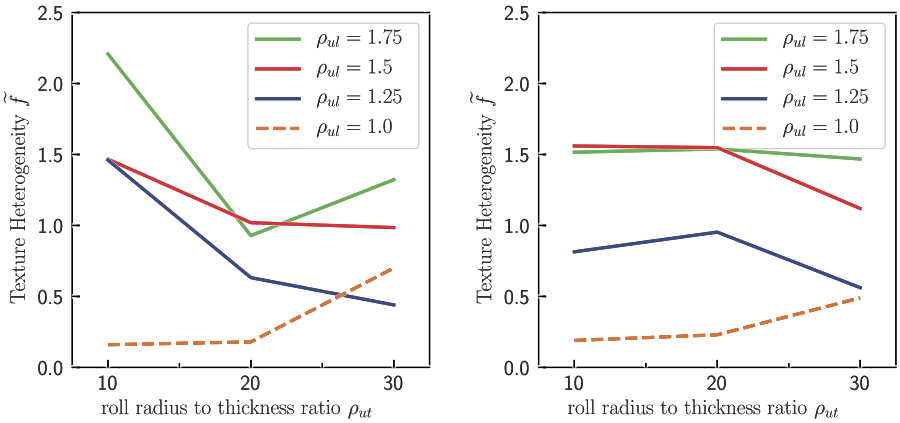

Fig. 10. Texture heterogeneity $\widetilde{f}$ (Eq. (43)) as a function of the roll-radius-to-sheet-thickness ratio ρ_{ut}, with reduction $\rho_{\mathrm{rr}} = 0.4$; (left) assuming the properties of AA6016-HR and (right) the properties of AA1050-CR.

anisotropy is visible at high asymmetry $\rho_{\mathrm{ul}} \geq 1.5$, where the β fibre is reduced more for the cold-rolled AA1050-CR material than for the warm rolled AA6016-HR material.

The results suggest that the texture homogeneity is more strongly affected by the roll-radius-to-sheet-thickness ratio than by the anisotropy. It also appears that it may be most beneficial to carry out ASR in the last stages of cold rolling, where the sheet will have inevitably acquired a strong β fibre texture, and the roll-radius-to-sheet-thickness ratio will tend to be higher due to the small sheet thickness at this stage. Conversely, carrying out ASR in the initial stage of cold rolling can be expected to be less effective due to the typical recrystallisation type texture present after hot rolling and the greater sheet thickness.

The second aspect that is examined is the influence of the anisotropy during ASR on the development of texture heterogeneity. As explained in the method section, the texture evolution is simulated as a function of position in the sheet thickness by calculating velocity gradients from the deformation field obtained from the FEA. This allows the texture heterogeneity to be quantified by Eq. (43) as $\widetilde{f}$. $\widetilde{f}$ is the maximum of the values of the squared difference of an ODF for a texture at a given position in the sheet thickness $f(g)_i$ with the average ODF for all of the textures at all thickness positions $f(g)_{\mathrm{avg}}$ – a large value of $\widetilde{f}$ indicates that a large texture gradient is present in a given simulated sheet.

$$\widetilde{f} = \max\left(\int \left(f(g)_i - f(g)_{\mathrm{avg}}\right)^2 \mathrm{d}g\right) \tag{43}$$

Fig. 10 plots $\widetilde{f}$ against the roll-radius-to-sheet-thickness ratio ρ_{ut}, for a reduction of $\rho_{\mathrm{rr}} = 40\%$. It is clear that symmetric rolling $\rho_{\mathrm{ut}} = 1$ is predicted to produce more homogeneous textures than ASR. It is also visible that increasing the asymmetry of the process tends to increase texture heterogeneity, but increasing the roll-radius-to-sheet-thickness ratio mitigates this effect. The influence of anisotropy suggests that lower values of $\widetilde{f}$ are obtained with the anisotropic properties of the

AA6016-HR material, but that for higher values of the ratio $\rho_{ut} = 30$, the differences in texture heterogeneity between the two materials is small.

3.3. Discussion

In terms of using ASR for modification of the texture in aluminium alloys, the pre-existing anisotropy of the sheet being rolled is predicted to most influence the texture evolution at higher process asymmetry (higher roll radius ratios). The material with the anisotropy arising from a sharp cold-rolled texture appears to result in the most beneficial texture modifications – i.e. greatest reduction in β fibre, greatest reduction in sensitivity of texture evolution to other process parameters. This is significant because it is beneficial to both increase the γ fibre, but to also decrease the β fibre. The γ fibre will tend to be stable during texture changes occurring during the annealing step at the end of cold rolling [31,32], while the β fibre will tend to transform to the cube orientation [107], which is detrimental to the anisotropy $\bar{r}$ and should be minimised.

The current implementation does not feature full coupling between the multiscale model, the FACET model and the FE code. As such, this has already been demonstrated using the general purpose FACET model by Gawad et al. [84], and the scope of the research presented here was rather to focus on the implementation of a 2D variant of the FACET method and its application to the parametric study of ASR. This of course implies that, in the present work, anisotropy is not updated during the simulation of deformation. This limitation would be problematic if multiple rolling passes were simulated, as would be the case in a commercial production environment, where the large strains developed would be expected to modify the texture and anisotropy very significantly. In the present case, it may be considered that the single reduction does not induce such large anisotropy changes that the trends observed above are invalidated.

From a more general simulation perspective, the FACET model is seen to be an effective method of capturing the anisotropic plasticity predicted by CP models – in Fig. 8, it is clear that the analytic FACET function accurately reproduces the discrete CP model results after calibration by virtual tests. It can be emphasised that the discrete points shown as the open circles in Fig. 8 are drawn from a vastly larger superset than those used in the calibration, which are themselves much more sparse and broadly distributed over the stress space.

It is important to reiterate that the FACET method is not limited to statistical CP models such as the ALAMEL model used here, but in fact would work in much the same way with more sophisticated and computationally heavy plasticity models such as CPFEM or CPFFT. The particular 2D stress space formulation of the FACET model presented here can be rapidly calibrated with as few as $\eta = 100$ virtual tests, which makes it suitable for use in a fully coupled multiscale modelling framework.

4. Conclusions

A parametric study was presented, which employs an anisotropic constitutive law in order to study the effect of anisotropic plasticity on the deformation field, and thus the evolution of the texture during the ASR process. A version of the FACET method is presented where a FACET function is restricted to the subspace of the stress and strain rate space relevant for 2D FEA. It is shown that such an approach can accurately reproduce the plastic anisotropy predicted by CP models (in this case, the ALAMEL model). It is expected that any plasticity model for which a convex yield surface exists and can be probed with virtual testing can be used with this approach.

In the results presented here, it is seen that the plastic anisotropy of the material undergoing ASR most strongly influences the deformation field and the texture evolution at high levels of process asymmetry (high values of roll radius ratio). It is seen that the anisotropy of a sharp cold-rolled type (β fibre) texture appears more beneficial than that of a recrystallisation (cube)-type texture. There is a less clear influence of anisotropy on the formation of texture gradients, and the ratio of roll-radius-to-sheet-thickness is a dominant process parameter, which agrees with earlier findings [106]. The results suggest that, from the point of view of promoting texture changes, it may be most beneficial to carry out ASR in the latest stages of cold rolling where the texture will tend to have developed a strong β fibre and where the roll-radius-to-sheet-thickness ratio will tend to be highest due to the reduced thickness of the sheet.

Acknowledgements

The authors wish to acknowledge the support of the KU Leuven IOF Knowledge Platform project KP/12/007, and the Research Foundation Flanders (FWO) and the Flemish Government, department EWI for provision of computational resources via the VSC (Flemish Supercomputer Center). Diarmuid Shore gratefully acknowledges the Flanders Innovation and Entrepreneurship Agency (VLAIO, formerly the Flemish government agency for Innovation by Science and Technology IWT) for provision of the doctoral scholarship number SB/121550.

References

[1] M. Goede, M. Stehlin, L. Rafflenbeul, G. Kopp, E. Beeh, Super Light Car – lightweight construction thanks to a multi-material design and function integration, Eur. Transp. Res. Rev. 1 (2009) 5–10.

[2] O. Engler, J. Hirsch, Texture control by thermomechanical processing of AA6XXAl–Mg–Si sheet alloys for automotive applications – a review, Mater. Sci. Eng. A 336 (2002) 249–262.

[3] J. Hirsch, Recent development in aluminium for automotive applications, Trans. Nonferr. Met. Soc. China 24 (2014) 1995–2002.
[4] G. Totten, D. MacKenzie, Handbook of Aluminium, Marcel Dekker Inc., 2003.
[5] S. Hirth, G. Marshall, S. Court, J. Lloyd, Effects of Si on the aging behaviour and formability of aluminium alloys based on AA6016, Mater. Sci. Eng. A 319–321 (2001) 452–456.
[6] J. Lian, F. Barlat, B. Baudelet, Plastic behaviour and stretchability of sheet metals. Part II: effect of yield surface shape on sheet forming limit, Int. J. Plast. 5 (1989) 131–147.
[7] H. Vegter, C. ten Horn, Y. An, Modeling of the plastic material behavior in advanced sheet metal forming simulations, in: R.K. Verma, D. Bhattachaejee (Eds.), Proceedings of the International Symposium of Automotive Sheet Metal Forming, Tata McGraw Hill Publishing Company Ltd., 2008, pp. 7–18.
[8] R. Whiteley, Importance of directionality in drawing quality sheet steel, Trans. Amer. Soc. Met. 154 (1960) 154–169.
[9] W. Lankford, S. Snyder, J. Bausher, New criteria for predicting the press performance of deep drawing sheets, Trans. Amer. Soc. Met. 42 (1950) 1197–1232.
[10] D. Leu, J. Wu, A simplified approach to estimate limiting drawing ratio and maximum drawing load in cup drawing, J. Eng. Mater. Technol. 126 (2004) 116–122.
[11] D. Leu, Prediction of the limiting drawing ratio and the maximum drawing load in cup-drawing, Int. J. Mach. Tools Manuf. 37 (1997) 201–213.
[12] P. Van Houtte, A. Van Bael, J. Winters, The incorporation of texture-based yield loci into elasto-plastic finite element programs, Textures Microstruct. 24 (1995) 255–272.
[13] J. Bishop, R. Hill, A theoretical derivation of the plastic properties of a polycrystalline face-centred metal, Philos. Mag. 42 (1951) 1298–1307.
[14] P. Van Houtte, S. Li, M. Seefeldt, L. Delannay, Deformation texture prediction: from the Taylor model to the advanced Lamel model, Int. J. Plast. 21 (2005) 589–624.
[15] J. Sidor, A. Miroux, R. Petrov, L. Kestens, Controlling the plastic anisotropy in asymmetrically rolled aluminium sheets, Philos. Mag. 88 (2008) 3779–3792.
[16] K. Kim, D. Lee, Analysis of deformation textures of asymmetrically rolled aluminum sheets, Acta Mater. 49 (2001) 2583–2595.
[17] S. Lee, D. Lee, Analysis of deformation textures of asymmetrically rolled steel sheets, Int. J. Mech. Sci. 43 (2001) 1997–2015.
[18] S. Kang, B. Min, H. Kim, D. Wilkinson, J. Kang, Effect of asymmetric rolling on the texture and mechanical properties of AA6111-aluminum sheet, Mater. Trans. 36 (2005) 3141–3149.
[19] B. Beausir, S. Biswas, D. Kim, L. Tóth, S. Suwas, Analysis of microstructure and texture evolution in pure magnesium during symmetric and asymmetric rolling, Acta Mater. 57 (2009) 5061–5077.
[20] J. Sidor, R. Petrov, L. Kestens, Texture induced anisotropy in asymmetrically rolled aluminium alloys, Adv. Eng. Mater. 13 (2011) 949–954.
[21] T. Sakai, K. Yoneda, S. Osugi, Microstructure and texture control of Al–Mg alloy sheets by differential speed rolling, Mater. Sci. Forum 495–497 (2005) 597–602.
[22] H. Jin, D. Lloyd, Evolution of texture in AA6111 aluminum alloy after asymmetric rolling with various velocity ratios between top and bottom rolls, Mater. Sci. Eng. A 465 (2007) 267–273.
[23] J. Lee, D. Lee, Texture control and grain refinement of AA1050 Al alloy sheets by asymmetric rolling, Int. J. Mech. Sci. 50 (2008) 869–887.
[24] J. Jiang, Y. Ding, F. Zuo, A. Shan, Mechanical properties and microstructures of ultrafine-grained pure aluminum by asymmetric rolling, Scr. Mater. 60 (2009) 905–908.
[25] B. Cheon, H. Kim, J. Lee, Asymmetric rolling of strip-cast Al–5.5Mg–0.3Cu alloy sheet: effects on the formability and mechanical properties, Mater. Sci. Eng. A 528 (2011) 5223–5227.
[26] S. Tamimi, J. Correia, A. Lopes, S. Ahzi, F. Barlat, J. Gracio, Asymmetric rolling of thin AA-5182 sheets: modelling and experiments, Mater. Sci. Eng. A 603 (2014) 150–159.
[27] J. Lee, G. Kim, S. Nam, I. Kim, D. Lee, Calculation of plastic strain ratio of AA1050 Al alloy sheet processed by heavy asymmetric rolling-annealing followed by light rolling-annealing, Comput. Mater. Sci. 100 (2015) 45–51.
[28] T. Sakai, S. Hamada, Y. Saito, Improvement of the r-value in 5052 aluminum alloy sheets having through-thickness shear texture by 2-pass single-roll drive unidirectional shear rolling, Scr. Mater. 44 (2001) 2569–2573.
[29] L. Tóth, B. Beausir, D. Orlov, R. Lapovok, A. Haldar, Analysis of texture and R value variations in asymmetric rolling of IF steel, J. Mater. Process. Technol. 212 (2012) 509–515.
[30] T. Zhang, Y. Wu, H. Gong, X. Zheng, S. Jiang, Effects of rolling parameters of snake hot rolling on strain distribution of aluminum alloy 7075, Trans. Nonferr. Met. Soc. China 24 (2014) 2150–2156.
[31] K. Kim, D. Lee, C. Choi, The deformation textures and lankford values of asymmetrically rolled aluminium alloy sheets, in: [109] 1999, pp. 755–760.
[32] O. Engler, H. Kim, M. Huh, Formation of {111} fibre texture in recrystallised aluminium sheet, J. Mater. Sci. Technol. 17 (2001) 75–86.
[33] L. Kestens, J. Sidor, R. Petrov, T. Nguyen Minh, Texture control in steel and aluminium alloys by rolling and recrystallization in non-conventional sheet manufacturing, Mater. Sci. Forum 715–716 (2012) 89–95.
[34] H. Kim, H. Kim, J. Cho, J. Lee, High-formability Al alloy sheet produced by asymmetric rolling of strip-cast sheet, Mater. Sci. Eng. A 574 (2013) 31–36.
[35] Y. Hwang, G. Tzou, An analytical approach to asymmetrical hot-sheet rolling considering the effects of the shear stress and internal moment at the roll gap, J. Mater. Process. Technol. 52 (1995) 399–424.
[36] H. Gao, S. Ramalingam, G. Barber, G. Chen, Analysis of asymmetrical cold rolling with varying coefficients of friction, J. Mater. Process. Technol. 124 (2002) 178–182.
[37] M. Salimi, M. Kadkhodaei, Slab analysis of asymmetrical sheet rolling, J. Mater. Process. Technol. 150 (2004) 215–222.
[38] W. Gong, Y. Pang, C. Liu, H. Yu, B. Lu, M. Zhang, Effect of asymmetric friction on front end curvature in plate and sheet rolling process, J. Iron Steel Res. Int. 17 (2010) 22–26.
[39] M. Qwamizadeh, M. Kadkhodaei, M. Salimi, Asymmetrical sheet rolling analysis and evaluation of developed curvature, Int. J. Adv. Manuf. Technol. 61 (2011) 227–235.
[40] S. Zhang, D. Zhao, C. Gao, G. Wang, Analysis of asymmetrical sheet rolling by slab method, Int. J. Mech. Sci. 65 (2012) 168–176.
[41] A. Halloumi, C.H. Desrayaud, B. Bacroix, E. Rauch, F. Montheillet, A simple analytical model of asymmetric rolling, Arch. Metall. Mater. 57 (2012) 425–435.
[42] A. Aboutorabi, A. Assempour, H. Afrasiab, Analytical approach for calculating the sheet output curvature in asymmetrical rolling: in the case of roll axis displacement as a new asymmetry factor, Int. J. Mech. Sci. 105 (2016) 11–22.
[43] R. Shivpuri, P. Chou, C. Lau, Finite element investigation of curling in non-symmetric rolling of flat stock, Int. J. Mech. Sci. 30 (1988) 625–635.
[44] A. Richelsen, Elastic–plastic analysis of the stress and strain distributions in asymmetric rolling, Int. J. Mech. Sci. 39 (1997) 1199–1211.
[45] A. Kawałek, Forming of band curvature in asymmetrical rolling process, J. Mater. Process. Technol. 155–156 (2004) 2033–2038.
[46] S. Mousavi, S. Ebrahimi, R. Madoliat, Three dimensional numerical analyses of asymmetric rolling, J. Mater. Process. Technol. 187–188 (2007) 725–729.
[47] M. Philipp, W. Schwenzfeier, F. Fischer, R. Wodlinger, C. Fischer, Front end bending in plate rolling influenced by circumferential speed mismatch and geometry, J. Mater. Process. Technol. 184 (2012) 224–232.
[48] L. Hao, H. Di, D. Gong, Analysis of sheet curvature in asymmetrical cold rolling, J. Iron Steel Res. Int. 20 (2013) 34–37.
[49] F. Farhatnia, M. Salimi, Effect of entry bending moment on exit curvature in asymmetrical rolling, Int. J. Eng. Sci. Technol. 3 (2011) 147–163.

[50] S. Wronski, B. Ghilianu, T. Chauveau, B. Bacroix, Analysis of textures heterogeneity in cold and warm asymmetrically rolled aluminium, Mater. Charact. 62 (2011) 22–34.
[51] S. Wronski, B. Bacroix, Microstructure evolution and grain refinement in asymmetrically rolled aluminium, Acta Mater. 76 (2014) 404–412.
[52] M. Moore, P. Bate, Microstructural inhomogeneity and biaxial stretching limits in aluminium alloy AA6016, J. Mater. Process. Technol. 125–126 (2002) 258–266.
[53] P. Bate, M. Moore, S. Court, Texture segregation and texture change in the biaxial stretching of AA6016, Mater. Sci. Forum 495–497 (2005) 585–590.
[54] J. Cho, H. Jeong, J. Szpunar, Effect of through thickness inhomogeneity of texture on edge cracking during planetary hot rolling of austenitic stainless steel, in: [109] 1999, pp. 1254–1259.
[55] J. Lenard, Metal Forming Science and Practice, Elsevier, 2002.
[56] P. Friedman, J. Pan, Effects of plastic anisotropy and yield criteria on prediction of forming limit curves, Int. J. Mech. Sci. 42 (2000) 29–48.
[57] S. Soare, Theoretical considerations upon the MK model for limit strains prediction: the plane strain case, strain-rate effects, yield surface influence, and material heterogeneity, Eur. J. Mech. A, Solids 29 (2010) 938–950.
[58] P. Eggertsen, K. Mattiasson, On constitutive modeling for springback analysis, Int. J. Mech. Sci. 52 (2010) 804–818.
[59] J. Yoon, F. Barlat, R. Dick, M. Karabin, Prediction of six or eight ears in a drawn cup based on a new anisotropic yield function, Int. J. Plast. 22 (2006) 174–193.
[60] G. Taylor, H. Quinney, The plastic distortion of metals, Philos. Trans. R. Soc. Lond., A 230 (1931) 323–362.
[61] R. Hill, A theory of the yielding and plastic flow of anisotropic metals, Proc. R. Soc. A 193 (1948) 281–297.
[62] J. Woodethorpe, R. Pearce, The anomalous behaviour of aluminium sheet under balanced biaxial tension, Int. J. Mech. Sci. 12 (1970) 341–347.
[63] R. Hill, Theoretical plasticity of textured aggregates, Math. Proc. Camb. Philos. Soc. 85 (1979) 179–191.
[64] D. Banabic, H. Bunge, K. Pöhlandt, A. Tekkaya, Formability of Metallic Materials, Springer, 2000.
[65] F. Barlat, O. Cazacu, M. Zyczkowski, D. Banabic, J.W. Yoon, Yield surface plasticity and anisotropy in sheet metals, in: [108] 2004, pp. 145–167.
[66] F. Chinesta, E. Cueto, Advances in Material Forming – Esaform 10 years on, Springer, 2007.
[67] F. Yoshida, H. Hamasaki, T. Uemori, A user-friendly 3D yield function to describe anisotropy of steel sheets, Int. J. Plast. 45 (2013) 119–139.
[68] S. Bruschi, T. Altan, D. Banabic, P. Bariani, A. Brosius, J. Cao, A. Ghiotti, M. Khraisheh, M. Merklein, A. Tekkaya, Testing and modelling of material behaviour and formability in sheet metal forming, CIRP Ann. Manuf. Technol. 63 (2014) 727–749.
[69] J. Betten, Applications of tensor functions to the formulation of yield criteria for anisotropic materials, Int. J. Plast. 4 (1988) 29–46.
[70] F. Barlat, J. Yoon, O. Cazacu, On linear transformations of stress tensors for the description of plastic anisotropy, Int. J. Plast. 23 (2007) 876–896.
[71] F. Barlat, D. Lege, J. Brem, A six-component yield function for anisotropic materials, Int. J. Plast. 7 (1991) 693–712.
[72] A. Karafillis, M. Boyce, A general anisotropic yield criterion using bounds and a transformation weighting tensor, J. Mech. Phys. Solids 41 (1993) 1859–1886.
[73] B. Plunkett, O. Cazacu, F. Barlat, Orthotropic yield criteria for description of the anisotropy in tension and compression of sheet metals, Int. J. Plast. 24 (2008) 847–866.
[74] R. Logan, W. Hosford, Upper-bound anisotropic yield locus calculations assuming ⟨111⟩-pencil glide, Int. J. Mech. Sci. 22 (1980) 419–430.
[75] P. Lequeu, P. Gilormini, F. Montheillet, B. Bacroix, J. Jonas, Yield surfaces for textured polycrystals–I. Crystallographic approach, Acta Metall. 35 (1987) 439–451.
[76] P. Van Houtte, K. Mols, B. Van Bael, E. Aernoudt, Application of yield loci calculated from texture data, Textures Microstruct. 11 (1989) 23–39.
[77] M. Arminjon, B. Bacroix, On plastic potentials for anisotropic metals and their derivation from the texture function, Acta Mech. 88 (1991) 219–243.
[78] B. Bacroix, P. Gilmorini, Finite element simulations of earing in polycrystalline materials using a texture adjusted strain rate potential, Model. Simul. Mater. Sci. Eng. 3 (1995) 1–21.
[79] M. Darrieulat, D. Piot, A method of generating analytical yield surfaces of crystalline materials, Int. J. Plast. 12 (1996) 575–610.
[80] P. Van Houtte, A. Van Bael, Convex plastic potentials of 4th and 6th rank for anisotropic materials, Int. J. Plast. 20 (2004) 1505–1524.
[81] P. Eyckens, H. Mulder, J. Gawad, H. Vegter, D. Roose, T. van den Boogaard, A. Van Bael, P. Van Houtte, The prediction of differential hardening behaviour of steels by multi-scale crystal plasticity modelling, Int. J. Plast. 73 (2015) 119–141.
[82] O. Cazacu, N. Chandola, B. Revil-Baudard, Analytical expressions for the yield stress and Lankford coefficients of polycrystalline sheets based on a new single crystal model, Int. J. Mater. Forming (2017), https://doi.org/10.1007/s12289-017-1366-3.
[83] P. Van Houtte, S.K. Yerra, A. Van Bael, The facet method: a hierarchical multilevel modelling scheme for anisotropic convex plastic potentials, Int. J. Plast. 25 (2009) 332–350.
[84] J. Gawad, A. Van Bael, P. Eyckens, G. Samaey, P. Van Houtte, D. Roose, Hierarchical multi-scale modeling of texture induced plastic anisotropy in sheet forming, Comput. Mater. Sci. 66 (2013) 65–83.
[85] H. Zhang, M. Diehl, F. Roters, D. Raabe, A virtual laboratory using high resolution crystal plasticity simulations to determine the initial yield surface for sheet metal forming operations, Int. J. Plast. 80 (2016) 111–138.
[86] J. Gawad, D. Banabic, A. Van Bael, D. Comsa, M. Gologanu, P. Eyckens, P. Van Houtte, D. Roose, An evolving plane stress yield criterion based on crystal plasticity virtual experiments, Int. J. Plast. 75 (2015) 141–169.
[87] K. Zhang, B. Holmedal, O. Hopperstad, S. Dumoulin, J. Gawad, A. Van Bael, P. Van Houtte, Multi-level modelling of mechanical anisotropy of commercial pure aluminium plate: crystal plasticity models, advanced yield functions and parameter identification, Int. J. Plast. 66 (2015) 3–30.
[88] W. Robert, D. Piot, J.H. Driver, A rapid deformation texture model incorporating grain interactions, Scr. Mater. 50 (2004) 1215–1219.
[89] P. Van Houtte, S. Li, O. Engler, Taylor-type homogenization methods for texture and anisotropy, in: [108] 2004, pp. 459–471.
[90] O. Engler, M. Crumbach, S. Li, Alloy-dependent rolling texture simulation of aluminium alloys with a grain-interaction model, Acta Mater. 53 (2005) 2241–2257.
[91] A. Molinari, G. Canova, S. Ahzi, A self-consistent approach of the large deformation polycrystal viscoplasticity, Acta Metall. 35 (1987) 2983–2994.
[92] R. Lebensohn, C. Tomé, A self-consistent anisotropic approach for the simulation of plastic deformation and texture development of polycrystals: application to zirconium alloys, Acta Metall. 41 (1993) 2611–2624.
[93] F. Roters, P. Eisenlohr, L. Hantcherli, D. Tjahjanto, T. Bieler, D. Raabe, Overview of constitutive laws, kinematics, homogenization, and multiscale methods in crystal plasticity finite element modeling: theory, experiments, applications, Acta Mater. 58 (2010) 1152–1211.
[94] R. Lebensohn, C. Tomé, P. Ponte Castañeda, Self-consistent modelling of the mechanical behaviour of viscoplastic polycrystals incorporating intragranular field fluctuations, Philos. Mag. 87 (2007) 4287–4322.
[95] F. Roters, P. Eisenlohr, C. Kords, D. Tjahjanto, M. Diehl, D. Raabe, DAMASK: the Düsseldork Advanced Material Simulation Kit for studying crystal plasticity using an FE based or spectral numerical solver, Proc. IUTAM 3 (2012) 3–10.
[96] P. Van Houtte, Application of plastic potentials to strain rate sensitive and insensitive anisotropic materials, Int. J. Plast. 10 (1994) 719–748.
[97] C. Lawson, R. Hanson, Solving Least Squares Problems, SIAM, 1995.
[98] E. Saff, A. Kuijlaars, Distributing many points on a sphere, Math. Intell. 19 (1997) 5–11.
[99] J. Sidor, R. Petrov, L. Kestens, Microstructural and texture changes in severely deformed aluminum alloys, Mater. Charact. 62 (2011) 228–236.
[100] M. Crumbach, M. Goerdeler, G. Gottstein, Modelling of recrystallisation textures in aluminium alloys: II. Model performance and experimental validation, Acta Mater. 54 (2006) 3291–3306.

[101] J.J. Sidor, K. Decroos, R.H. Petrov, L.A.I. Kestens, Evolution of recrystallization textures in particle containing Al alloys after various rolling reductions: experimental study and modeling, Int. J. Plast. 66 (2015) 119–137.
[102] I.L. Dillamore, W.T. Roberts, Rolling textures in fcc and bcc metals, Acta Metall. 12 (1964) 281–293.
[103] L.A.I. Kestens, H. Pirgazi, Texture formation in metal alloys with cubic crystal structures, Mater. Sci. Technol. 32 (2016) 1303–1315.
[104] T. Kuwabara, A. Van Bael, E. Iizuka, Measurement and analysis of yield locus and work hardening characteristics of steel sheets with different r-values, Acta Mater. 50 (2002) 3717–3729.
[105] Simulia Ltd., Abaqus Theory Guide 6.13. Dassault Systèmes, 2013.
[106] D. Shore, L. Kestens, J. Sidor, P. Van Houtte, A. Van Bael, Process parameter influence on texture heterogeneity in asymmetric rolling of aluminium sheet alloys, Int. J. Mater. Forming 11 (2016) 297–309, https://doi.org/10.1007/s12289-016-1330-7.
[107] J. Hirsch, T. Al-Samman, Superior light metals by texture engineering: optimized aluminum and magnesium alloys for automotive applications, Acta Mater. 61 (2013) 818–843.
[108] D. Raabe, L.D. Chen, F. Barlat, F. Roters (Eds.), Continuum Scale Simulation of Engineering Materials, Wiley, 2004.
[109] J. Szpunar (Ed.), Proceedings of the Twelfth International Conference on Textures of Materials, ICOTOM 12, NRC Research Press, 1999.